



저작자표시-비영리-변경금지 2.0 대한민국

이용자는 아래의 조건을 따르는 경우에 한하여 자유롭게

- 이 저작물을 복제, 배포, 전송, 전시, 공연 및 방송할 수 있습니다.

다음과 같은 조건을 따라야 합니다:



저작자표시. 귀하는 원저작자를 표시하여야 합니다.



비영리. 귀하는 이 저작물을 영리 목적으로 이용할 수 없습니다.



변경금지. 귀하는 이 저작물을 개작, 변형 또는 가공할 수 없습니다.

- 귀하는, 이 저작물의 재이용이나 배포의 경우, 이 저작물에 적용된 이용허락조건을 명확하게 나타내어야 합니다.
- 저작권자로부터 별도의 허가를 받으면 이러한 조건들은 적용되지 않습니다.

저작권법에 따른 이용자의 권리는 위의 내용에 의하여 영향을 받지 않습니다.

이것은 [이용허락규약\(Legal Code\)](#)을 이해하기 쉽게 요약한 것입니다.

[Disclaimer](#)

이학박사 학위논문

Facile strategies to improve the economy
of polymer synthesis and self-assembly

고분자 합성과 자기 조립 현상의
경제성을 향상시키는 손쉬운 전략

2016년 2월

서울대학교 대학원
화학부 고분자화학 전공
이 인 환

Abstract

Facile strategies to improve the economy of polymer synthesis and self-assembly

In-Hwan Lee

Department of Chemistry

The Graduate School

Seoul National University

Preparation of polymers and their self-assembled nanostructures with high controllability, efficiency, and economy is central basis for the development of polymeric nanomaterials. To address this issue, following four chapters described facile strategies for the synthesis and self-assembly of polymers with economic consideration.

Chapter 2 described the concept of **step-economic** in situ nanoparticlization of conjugated polymers (INCP) with addressing the effect of core forming block. Poly(*para*-phenylene) was used as first block, and highly insoluble polythiophene or poly(3-methylthiophene) was used as second block to induce in situ self-assembly. We found that solubility and packing mode of second block were important factors to determine nanostructures.

Chapter 3 described **step-economic** in situ nanoparticlization of conjugated polymers with addressing the effect of shell forming block. Poly(3-alkylthiophene)

was used as first block, and highly insoluble polythiophene was used as second block to induce in situ self-assembly. It was found that hydrodynamic volume of first block and well-defined polymer structure were important factors to modulate the shape of nanostructures.

Chapter 4 presented the **price-economic** synthesis of the conjugated polymers using recyclable Pd-Fe₃O₄ heterodimer nanocrystal. AB-alternating copolymers were synthesized by Suzuki-Miyaura polycondensation with Pd-Fe₃O₄ nanocrystals. Significantly, Pd-Fe₃O₄ bimetallic nanocrystals were easily recovered by magnet and recyclable with minimal Pd leaching.

Chapter 5 reported the **atom and step-economic** synthesis of poly(*N*-sulfonylamidine)s using Cu-catalyzed multicomponent polymerization. Optimization of polymerization condition enabled the synthesis of poly(*N*-sulfonylamidine) with high molecular weight and yield. Furthermore, this polymerization expanded to the library synthesis of poly(*N*-sulfonylamidine). This research is significant because this polymerization overcome previous limitations such as low molecular weight, defect in polymer structure, and narrow substrate scope.

In summary, this thesis described economic synthesis of polymers and self-assembled nanostructures via INCP, heterogeneous catalysis, and multi-component polymerization. We believe that these strategies will expand their scope and suggest a new platform for the preparation of useful nanomaterials.

keywords: in situ nanoparticlization of conjugated polymers, recyclable Pd-Fe₃O₄ heterodimer nanocrystal, Cu-catalyzed multicomponent polymerization

Student Number: 2010-20288

Table of Contents

Abstract	p.i
Chapter 1. Introduction to in situ nanoparticlization of conjugated polymer (INCP)	p.1
Introduction	p.2
In situ nanoparticlization of conjugated polymers (INCP)	p.3
Previous examples of INCP and thesis research	p.5
Chapter 2. In situ nanoparticlization of fully conjugated block copolymers using Grignard Metathesis method: Effect of core block	p.7
Background	p.8
Part I. In situ nanoparticlization of PPP- <i>b</i> -PT	p.9
Part II. In situ nanoparticlization of PPP- <i>b</i> -P3MT	p.16
Part III. In situ nanoparticlization of PPP- <i>b</i> -P(3MT- <i>ran</i> -T)	p.27
Chapter 3. In situ nanoparticlization of fully conjugated block copolymers using Grignard Metathesis method: Effect of shell block	p.34
Background	p.35
Part I. In situ nanoparticlization of P3EHT- <i>b</i> -PT	p.36
Part II. In situ nanoparticlization of P3ODT- <i>b</i> -PT	p.45
Part III. In situ nanoparticlization of PTPP- <i>b</i> -PT	p.50

Part IV. In situ nanoparticlization of P3HT-*b*-PT using externally
initiating precatalyst p.53

**Chapter 4. Pd-Fe₃O₄ heterodimer nanocrystal-catalyzed Suzuki-
Miyaura polycondensation** p.60

**Chapter 5. Cu-catalyzed multicomponent polymerization:
Synthesis of Poly(*N*-sulfonylamidine)** p.71

Chapter 1

Introduction to in situ nanoparticlization of conjugated polymers (INCP)

Introduction

Development of living polymerization was one of the breakthroughs in the history of polymer science.¹ One of advances starting from living polymerization was the well-controlled synthesis of block copolymers which have two distinct blocks linked by covalent bond. With the appearance of block copolymers in the field of polymer chemistry, self-assembly of block copolymers started to take great attention not only due to its interesting phenomenon but also due to the demand for functional nanomaterials. Specifically, the first report for self-assembly of block copolymers, e.g. polystyrene-*b*-poly(methyl methacrylate) (PS-*b*-PMMA), demonstrated the formation of nanospheres.² Thereafter, self-assembly of block copolymers has been developed greatly being able to access to various type of nanostructures in solution and film state.³ Although these self-assembly processes of block copolymers have been advanced greatly, their self-assembly processes could be advanced more by judicious design of block copolymers as well as development of self-assembly conditions. What we observed in conventional self-assembly processes was that it needed time-demanding post-synthetic treatments such as selective solvent addition and aging (Figure 1.1), because block copolymer itself did not have any driving force to be assembled. Moreover, resulting nanostructures were unstable toward outer condition change (Figure 1.1). This phenomenon could be useful for stimuli-responsive ‘smart materials’, however, generally this instability means degradation or disassembly of nanomaterials. In addition, this instability might be bad for

optoelectronic devices which need long-term stability.

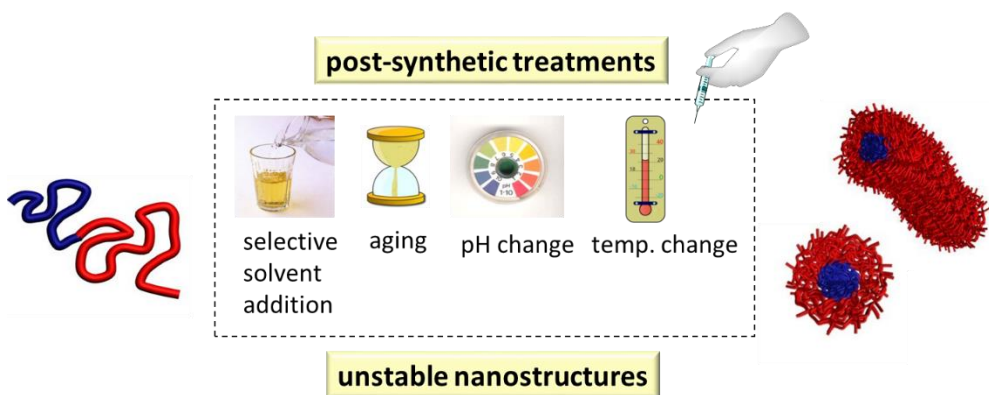
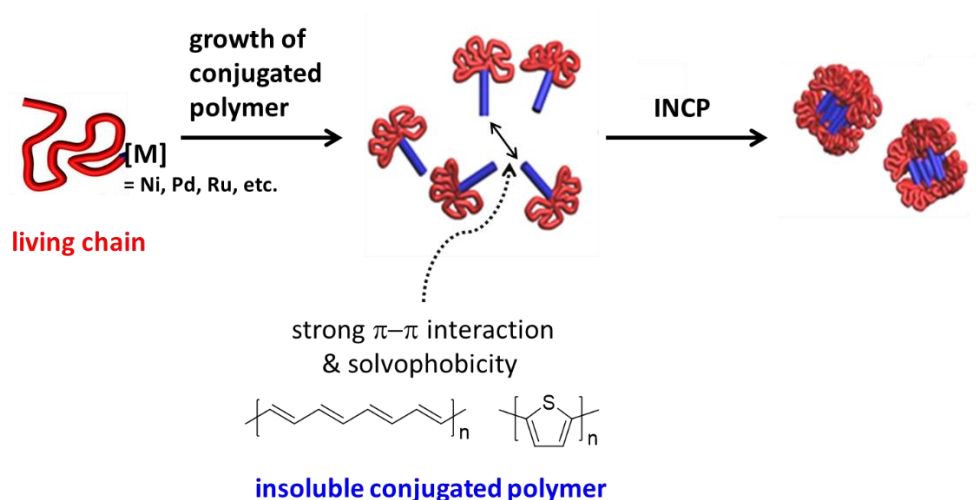


Figure 1.1. Conventional self-assembly of preformed polymers in solution via post-synthetic treatments

In situ nanoparticlization of conjugated polymer (INCP)

To overcome the requirement of post-synthetic treatments and instability of nanostructures in conventional self-assembly processes, we designed a new process entitled “In situ nanoparticlization of conjugated polymer (INCP)”. This INCP needed two prerequisites to realize the concept. First one is living polymerization to be able to be used for the synthesis of conjugated polymers (Scheme 1.1). Second one is highly insoluble conjugated polymers which are used as second block during block copolymerization (Scheme 1.1). With these two prerequisites, one could design any of block copolymers containing highly insoluble conjugated polymers as second block for INCP process.

Scheme 1.1. Schematic demonstration of *in situ* nanoparticlization of conjugated polymers (INCP)



INCP first started from living polymerization of soluble first block (Scheme 1.1). When monomers for insoluble conjugated polymers were added into the soluble polymer chains with living chain-end, insoluble conjugated polymers were formed (Scheme 1.1). During the polymerization of highly insoluble conjugated polymers, when second block reached to solubility limit, they might start to assemble each other because of solvophobicity or strong $\pi-\pi$ interaction of highly insoluble conjugated polymer chains (Scheme 1.1). Finally, nanostructures of block copolymers were formed during the polymerization (Scheme 1.1). Overall, this nanostructure formation occurred during the polymerization without any post-treatments. Moreover, obtained nanostructures might be stable due to the strong $\pi-\pi$ interaction or high solvophobicity of second conjugated polymers.

Nanostructures from INCP could enrich the shape of nanostructures under kinetic or thermodynamic control. Moreover, utilizing well-defined nanostructures containing highly insoluble conjugated polymers as electronic materials has not been demonstrated yet. We believe that this new in situ self-assembly process could be useful for the generation of functional nanomaterials in step-economic manner.

Previous examples of in situ nanoparticlization of conjugated polymer (INCP) and thesis research

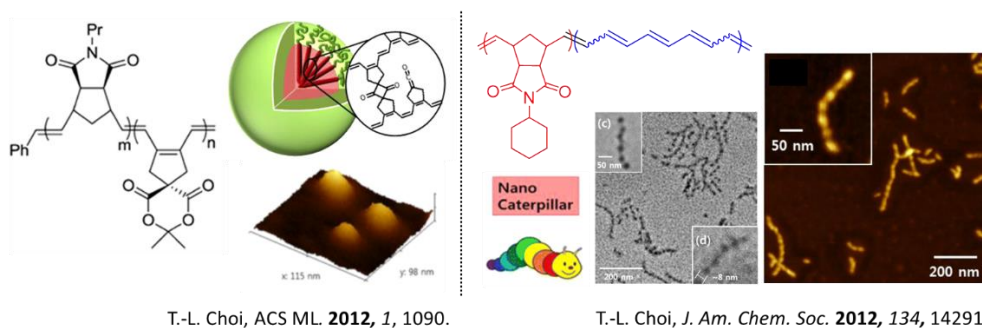


Figure 1.2. Two early examples of INCP using olefin metathesis polymerization as living polymerization and polyacetylene as highly insoluble second block

First two examples for INCP were demonstrated by our group in 2012.⁴⁻⁵ In these two examples, olefin metathesis polymerizations, i.e. ring-opening metathesis polymerization and cyclopolymerization, were used as living polymerization methods. And insoluble second blocks, polyacetylene and its derivatives, were used to induce in situ self-assembly. Interestingly, in situ nanoparticlization of polynorbornene-*block*-polyacetylene diblock copolymer (PN-*b*-PA) formed unique

nanocaterpillar structures in one-step.⁴ However, the first block PN was insulating which could be bad for charge transport in optoelectronic application, and PA was sensitive to oxidation. Thus, to improve the conductivity and stability for oxidation, we designed highly stable fully conjugated block copolymers for INCP. In this thesis, Chapter 2 and Chapter 3, we described in situ nanoparticlization of fully conjugated block copolymers for the formation of stable nanoparticles.

References

- (1) Szwarc, M. *Nature* **1956**, *178*, 1168.
- (2) Newman, S. *J. Appl. Polym. Sci.* **1962**, *6*, S15.
- (3) Bucknall, D. G.; Anderson, H. L. *Science* **2003**, *302*, 1904.
- (4) Yoon, K.-Y.; Lee, I.-H.; Kim, K. O.; Jang, J.; Lee, E.; Choi, T.-L. *J. Am. Chem. Soc.* **2012**, *134*, 14291.
- (5) Kim, J.; Kang, E.-H.; Choi, T.-L. *ACS Macro Lett.* **2012**, *1*, 1090.

Chapter 2

In situ nanoparticlization of fully conjugated block copolymers using Grignard Metathesis method: Effect of core block

Background

Conjugated polymer is a special kind of polymers conducting electricity. The conjugated polymers have been greatly attracted many attention due to their conductivity, softness, and solution processability, which leads to the promising new field, organic electronics. In line with this attention, synthesis of conjugated polymers has been greatly developed with the boom and understanding of small molecule coupling-reactions based on organometallic chemistry. Significantly, development and understanding of living polymerization method enabled the new application for the block copolymer formation with well-defined architecture. Moreover, the block copolymer themselves could be self-assembled under specific conditions leading to interesting nanostructures such as spherical and cylindrical micelles and vesicles. However, the self-assembly of the fully conjugated block copolymer itself was not much reported compared to that of non-conjugated block copolymers despite of the high potential applicability of conjugated nanostructures from organic polymers into organic electronics. In addition, when we look into the reported self-assembly processes of the fully conjugated block copolymers, they inevitably needed time-demanding post-synthetic treatments such as dilution, solvent composition change, *etc.*, because their designed block copolymer architecture didn't have any intrinsic driving force for the self-assembly during the polymerization. Furthermore, when we think of the stability of nanostructures from above mentioned block copolymers, their stability under condition change should be weak, because self-assembly only occurred in very narrow range of specific conditions. Therefore, overcoming these

challenge such as post-synthetic treatment process in conventional self-assembly and instability of resulting nanoparticles, in situ nanoparticlization of conjugated polymers (INCP), driven by exclusively high solvophobicity or π - π interaction of pristine conjugated polymers such as side-chain free polythiophene was envisioned.¹⁻

⁷ Indeed, the resulting nanoparticles were not only spontaneously formed during the polymerization without any post-treatment but also highly stable under stresses such as temperature change and sonication.¹⁻⁷ In this chapter, as an exemplary system, in situ nanoparticlization of the fully conjugated block copolymers containing poly(2,5-dialkyloxy-1,4-phenylene) first block with polythiophene or poly(3-methylthiophene) second block is described.⁴

Part I. In situ nanoparticlization of poly(2,5-dihexyloxy-1,4-phenylene)-*block*-polythiophene (PPP-*b*-PT)

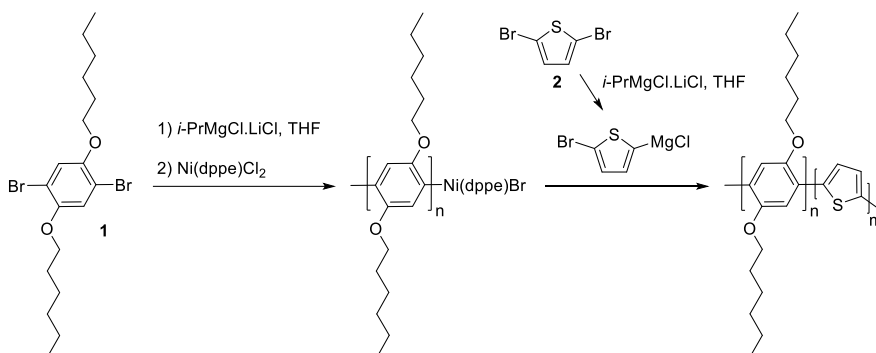
Introduction

Ring-opening metathesis polymerization (ROMP), catalyzed by Ru-based Grubbs catalysts, is an effective synthetic approach for access to various polymers with well-defined structures.⁸ In particular, the simplest conjugated polymer, polyacetylene (PA), was also synthesized by ROMP. However, controlled polymerization and block copolymer formation of PA by ROMP was not previously achieved due to the backbiting issue forming highly stable benzene as byproduct. At this stage, we focused on two main issues, i.e. overcoming the synthetic culprit for

ROMP of PA and step-economic in situ nanoparticlization of diblock copolymers containing PA. Indeed, as the first example of INCP, polynorbornene-*block*-polyacetylene (PN-*b*-PA) obtained through ROMP catalyzed by 3rd Generation Grubbs catalyst, formed well-defined nanocaterpillar structures during the polymerization under kinetic control.¹ However, the resulting PN-*b*-PA nanoparticles (NPs) have two intrinsic limitations originated from the corresponding block copolymer structure. First, PN shell is an insulating polymer, hampering the transport of charge current. Second, PA core is sensitive to air-oxidation resulting in loss of conjugation. Thus, as an alternative system, we focused on the charge conducting polymers with high air-stability like polythiophene and polyphenylene for the stable and conducting nanomaterial. Herein, we report the synthesis and in situ nanoparticlization of fully conjugated block copolymers containing polyphenylene first block with polythiophene second block.⁴

Results and Discussions

Table 2.1. Synthesis of PPP-*b*-PT by the GRIM method



entry	Ni(dppe)Cl ₂ :1:2	<i>M_n</i> (PDI) of PPP ^a	DP of PT ^b	yield
1	1:70:30	9.9k (1.26)	14	39%
2	1:70:55	10.4k (1.26)	37	51%
3	1:70:70	12.5k (1.35)	56	61%
4	1:70:90	10.1k (1.16)	76	42%

^aMeasured by THF size exclusion chromatography calibrated using polystyrene standards.

^bEstimated by gas chromatography-mass spectrometry.

As the in situ nanoparticlization of the full conjugated block copolymers in mind, poly(2,5-dihexyloxy-1,4-phenylene)-*block*-polythiophene (PPP-*b*-PT) was designed. Various ratio of PPP-*b*-PTs were effectively synthesized by a quasi-living Grignard metathesis (GRIM) method (Table 2.1).^{4,9-10} The ratio of Ni(dppe)Cl₂ to monomer **1** was fixed to 1:70 leading to *M_n* of PPP first block near 10 kg/mol with narrow poly dispersity indices (PDI, 1.15–1.35) in all cases, while the ratio of Ni(dppe)Cl₂ to monomer **2** was varied from 1:30 to 1:90 resulting in different length of second block from 14 to 76 (Table 2.1).

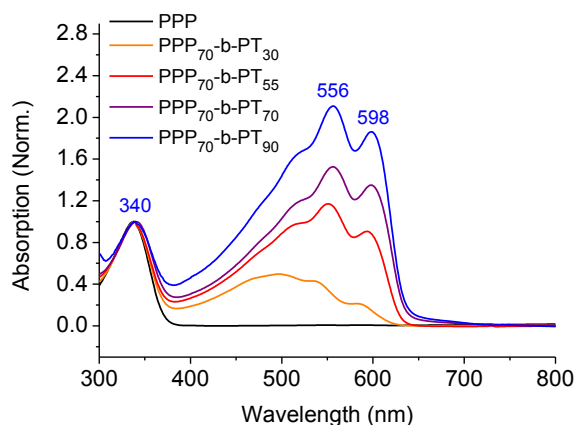


Figure 2.1. UV-vis spectra of PPP-*b*-PT in chloroform at room temperature

Peak position shift in size exclusion chromatography (SEC) was general method to identify the successful block copolymerization; however, in this INCP case, this SEC technique was not available. That is because, in situ nanoparticlization of conjugated polymers only provided nanostructures which disassembly into single-chain is virtually impossible. Moreover, the resulting nanostructures filtered by a guard column of SEC, which was pity to check the success of block copolymerization. As an alternative, we further checked the successful block copolymerization and micellization with UV-vis spectroscopy and ^1H NMR analysis. Firstly, block copolymer formation was confirmed by color change during the polymerization (yellow to deep purple) and UV-vis spectroscopy showing two distinct absorption peaks at 340 and 556 nm corresponding to the absorption of PPP and PT, respectively (Figure 2.1). Moreover, after the polymerization, only soluble particles were existed in organic solvents such as chloroform, indicating the lack of chain-transfer reaction

leading to insoluble PT. The completely identical ^1H NMR spectra between PPP homopolymer and PPP-*b*-PT block copolymer implied the formation of core-shell type micelles.⁴ Furthermore, vibronic peaks at 556 and 598 nm in UV-vis spectra in chloroform indicated that the core of micelle is highly ordered probably due to the strong π - π interaction existing even in solution (Figure 2.1).¹¹⁻¹²

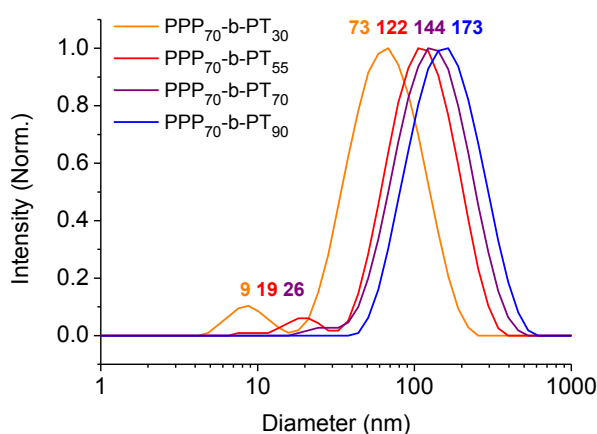
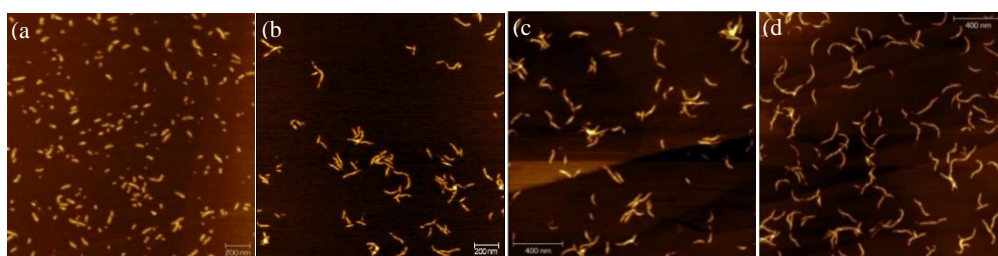


Figure 2.2. DLS profiles of nanocrystals from PPP-*b*-PT in chloroform at 20 °C



	PPP ₇₀ - <i>b</i> -PT ₅₅	PPP ₇₀ - <i>b</i> -PT ₇₀	PPP ₇₀ - <i>b</i> -PT ₉₀
L_n (L_w/L_n)	76 nm (1.13)	102 nm (1.25)	121 nm (1.16)
Height (H)	5.3 nm	6.4 nm	6.8 nm

Figure. 2.3. AFM images of the nanostructures from PPP-*b*-PT on HOPG: (a) PPP₇₀-*b*-PT₃₀, (b) PPP₇₀-*b*-PT₅₅, (c) PPP₇₀-*b*-PT₇₀, and (d) PPP₇₀-*b*-PT₉₀

To investigate the mechanism of in situ nanoparticlization of PPP-*b*-PT, series of nanoparticles (NPs) from PPP-*b*-PT were compared with each other. Actual size and shape of each nanostructures were identified by dynamic light scattering (DLS), atomic force microscopy (AFM) and transmission electron microscopy (TEM). Interestingly, the size of NPs increased from 73 to 173 nm as increasing the length of PT from 14 to 76 (Figure 2.2). Moreover, AFM images of PPP-*b*-PTs showed the initial nanosphere and short nanorod ($L_n = 76$ nm, $H = 5.3$ nm) elongated into longer nanorod ($L_n = 121$ nm, $H = 6.8$ nm) with concomitant increment of height of NPs (Figure 2.3). One notable thing is that length distribution (L_w/L_n) of NPs is quite narrow (1.13–1.25) (Figure 2.3).

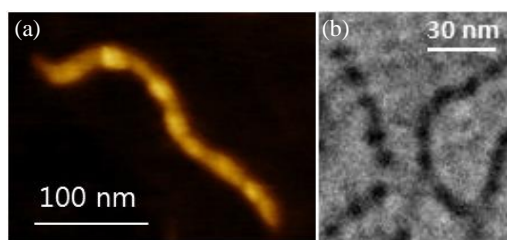


Figure 2.4. Nanocaterpillar structures from PPP-*b*-PT confirmed by (a) high-resolution AFM imaging and (b) magnified TEM imaging

High-resolution AFM and TEM images showed that these nanorod is undulated ones which formation is probably originated from the attachment of each nanospheres and short nanorods (Figure 2.4). In contrast to a common cylindrical micelles made by fusion of NPs and subsequent rearrangement of block copolymers,

NPs from INCP did not undergo rearrangement process presumably due to the immobile PT core trapped by high solvophobicity or strong π - π interaction.

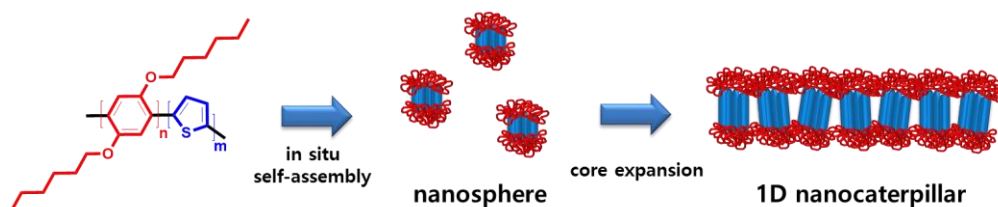


Figure 2.5. Proposed mechanism for the formation of nanosphere and 1D nanocaterpillar structures via in situ nanoparticlization of PPP-*b*-PT

Based on the various analyses presented above, we propose INCP mechanism for the synthesis of nanocaterpillar structure from PPP-*b*-PT (Figure 2.5). At first, PPP-*b*-PT initially self-assembled into nanospheres (Figure 2.5). As the DP of PT increases during the polymerization, the core expands, and larger area of the solvophobic PT core is exposed to the solvent (Figure 2.5). To minimize this unfavorable solvation, the nanospheres with exposed cores would cling to each other by strong π - π interactions, thereby forming the nanocaterpillar structures (Figure 2.5). We believe that uncontrolled branching did not occur because the PPP shell effectively solvates the expanded PT core.

Conclusion

In conclusion, we have demonstrated the synthesis of highly stable 1D nanocaterpillar crystals from fully conjugated PPP-*b*-PTs via INCP. With an increase in the DP of PT, the morphology of the nanostructures evolved from nanospheres to nanocaterpillar structures, and the length of the nanocaterpillar could also be controlled.

Part II. In situ nanoparticlization of poly(2,5-dihexyloxy-1,4-phenylene)-*block*-poly(3-methylthiophene) (PPP-*b*-P3MT)

Introduction

With the successful fabrication of nanocaterpillar structures via in situ nanoparticlization of PPP-*b*-PT, we are curious about factors affecting to INCP such as solvent and structure of polymers. At first, we decided to investigate the impact of structural factors of the second block on INCP. As an exemplary system, poly(2,5-dihexyloxy-1,4-phenylene)-*block*-poly(3-methylthiophene) (PPP-*b*-P3MT) were prepared by the same GRIM method, which was previously used for the synthesis of PPP-*b*-PT. In this part II, we describe the study for in situ nanoparticlization of PPP-*b*-P3MT,¹³ and this was compared to in situ nanoparticlization of previous PPP-*b*-PT⁴.

Results and Discussions

P3MT was chosen as a new core-forming second block, because it might be more soluble than the previous PT but still insoluble and crystalline enough for the direct in situ self-assembly, which might increase the length of nanocaterpillars. Moreover, crystallinity of P3MT (π -stacked packing) is quite different with that of PT (herringbone packing) (Scheme 2.1).¹⁴⁻¹⁶ Thus, with these factors in mind, we started a journey in the world of in situ nanoparticlization of PPP-*b*-P3MT.

Scheme 2.1. Comparison between In Situ Nanoparticlization of PPP-*b*-P3MT and PPP-*b*-PT. Note the Different Solubility and Packing Modes of P3MT and PT

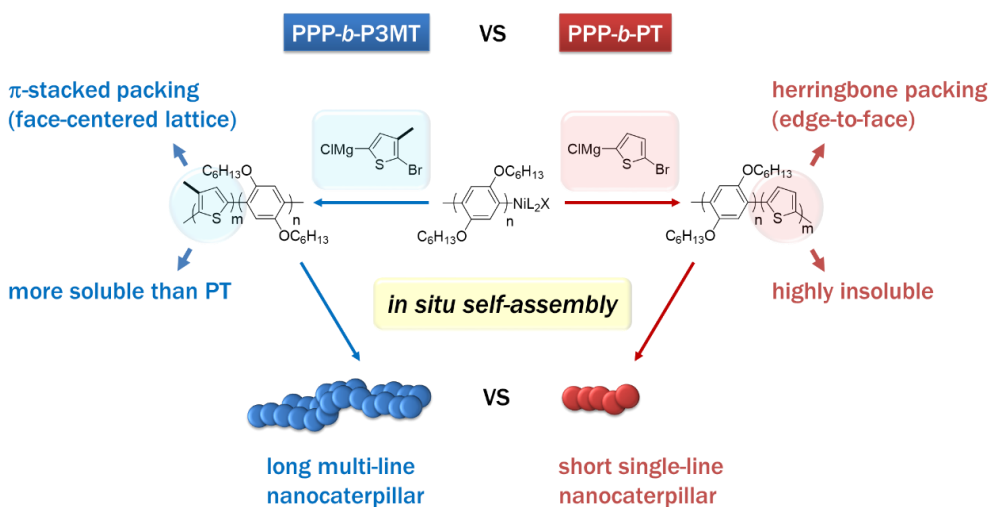
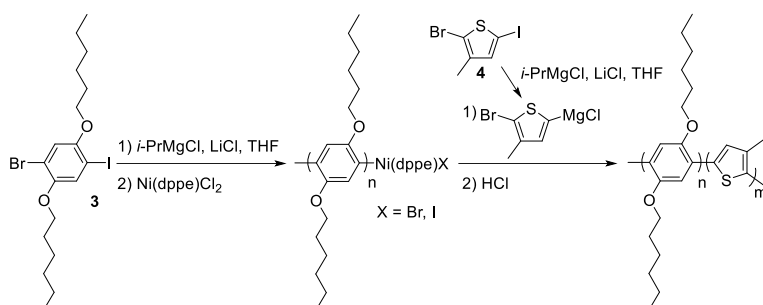


Table 2.2. Synthesis of PPP-*b*-P3MT by the Grignard Metathesis Polymerization Method



entry	Ni(dppe)Cl ₂ : 3 : 4	<i>M_n</i> (PDI) of PPP ^a	DP of P3MT ^b	yield
1	1 : 70 : 50	25.8k (1.06)	36	72%
2	1 : 70 : 115	25.0k (1.06)	84	73%
3	1 : 70 : 180	21.6k (1.04)	148	64%

^a Measured by THF size exclusion chromatography calibrated using polystyrene standards.

^b Estimated by gas chromatography-mass spectrometry.

The synthesis of three PPP-*b*-P3MTs was achieved by GRIM method (Table 2.2).⁹⁻¹⁰ Although previous PPP-*b*-PT was also synthesized by the same method,⁴ we found two factors to improve the synthesis. First, use of 1-bromo-4-iodo-2,5-dihexyloxybenzene (**3**) in the polymerization afforded PPP with better control over molecular weight, poly dispersity, and yield than the use of 1,4-dibromo-2,5-dihexyloxybenzene (**1**) as starting monomer.¹³ Second, addition of 1 equiv. of lithium chloride (LiCl) during the preparation of Grignard monomer from 2-bromo-5-iodo-3-methylthiophene was crucial for successful block copolymerization.¹³

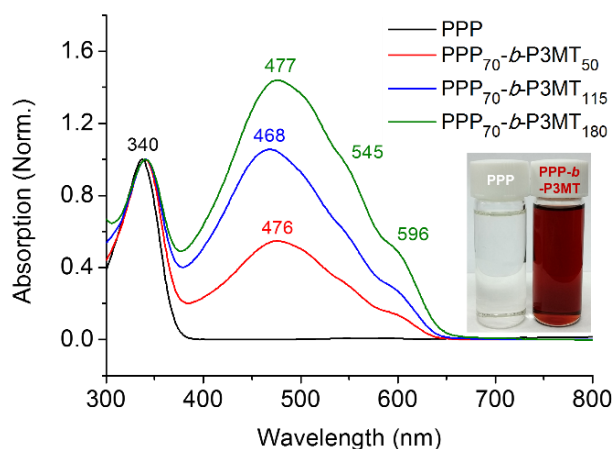
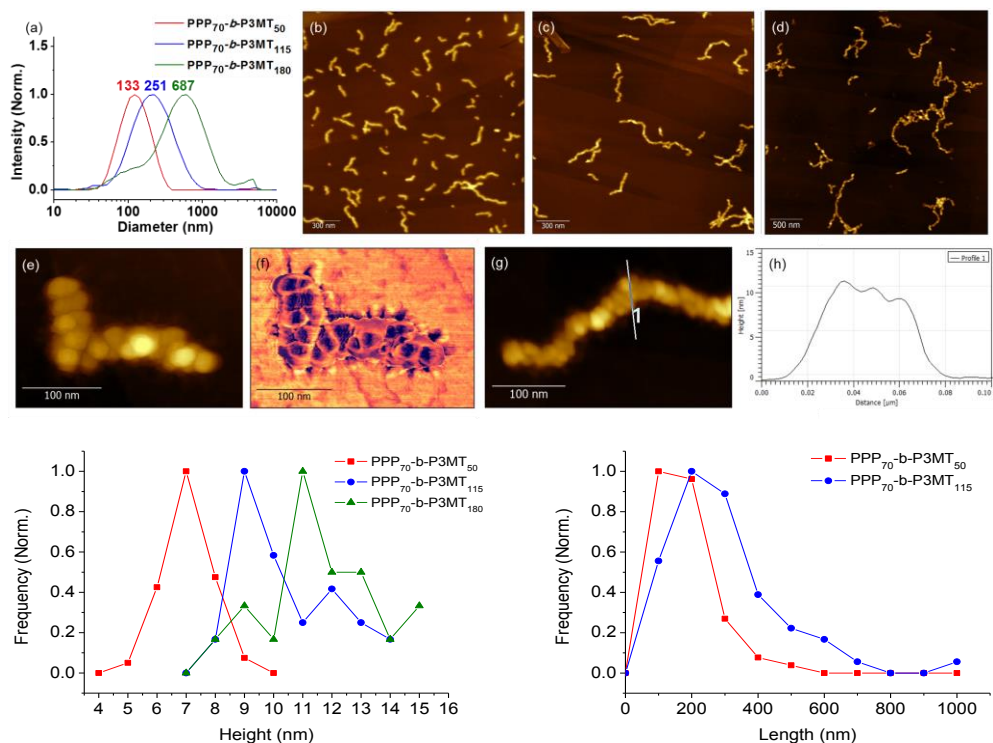


Figure 2.6. UV-vis spectra of PPP and PPP-*b*-P3MTs in chloroform at room temperature

At first, obtained polymers were analyzed by ^1H NMR spectroscopy and UV-vis spectra of PPP-*b*-P3MT. The ^1H NMR spectra of PPP homopolymer and PPP-*b*-P3MTs were identical as previous examples of INCP demonstrated.¹⁻⁷ Regarding the color of polymers, PPP in CHCl_3 was transparent, while PPP-*b*-P3MT in CHCl_3 showed brick-red color (Figure 2.6.). UV-vis spectra of PPP-*b*-P3MTs showed two distinct absorption at 340 nm and 477 nm, which were absorption of PPP and P3MT, respectively (Figure 2.6.). Moreover, there were distinct vibronic peaks at 545 and 596 nm even in CHCl_3 , and the intensity of vibronic peaks enhanced as increasing DP of PT (Figure 2.6.). All these observations for PPP-*b*-P3MT suggested the successful block copolymerization and core-shell type nanoparticle formation. Note that these phenomena of PPP-*b*-P3MTs are as similar as previous PPP-*b*-PTs⁴, however, vibronic peak and λ_{max} for PPP-*b*-PTs were much stronger and red-shifted than those of PPP-*b*-P3MTs (Figure 2.1. and Figure 2.6.).



	PPP ₇₀ -b-P3MT ₅₀	PPP ₇₀ -b-P3MT ₁₁₅	PPP ₇₀ -b-P3MT ₁₈₀
L_n	130 nm	246 nm	n.d.
L_w/L_n	1.45	1.47	n.d.
<i>Height (STDEV)</i>	6.6 nm (0.7 nm)	9.9 nm (1.7 nm)	11.2 nm (1.9 nm)

Figure 2.7. (a) DLS profiles of PPP-*b*-P3MT nanoparticles in chloroform at 20 °C. AFM images of the nanostructures from PPP-*b*-P3MTs on HOPG: (b) PPP₇₀-*b*-P3MT₅₀, (c) PPP₇₀-*b*-P3MT₁₁₅, and (d) PPP₇₀-*b*-P3MT₁₈₀. High-resolution AFM (e) height and (f) phase images of the nanostructures from PPP₇₀-*b*-P3MT₁₁₅. (g) High-resolution AFM image and (h) height profile of the nanostructure from PPP₇₀-*b*-P3MT₁₁₅.

The size and shape of nanoparticles from PPP-*b*-P3MTs were analysed the techniques with dynamic light scattering (DLS), atomic force microscopy (AFM) and transmission electron microscopy (TEM). The size of nanoparticles from PPP-*b*-

P3MTs increased from 133 to 687 nm as increasing DP of P3MT from 36 to 148 (Figure 2.7a). Moreover, height of nanoparticles also increased from 6.6 to 11.2 nm with increase the DP of P3MT (Figure 2.7). This size and height increment of nanoparticles was also as similarly observed from PPP-*b*-PTs (Figure 2.9). However, the extent for increase of size and height was larger for PPP-*b*-P3MT compared to PPP-*b*-PT (Figure 2.7 and Figure 2.9). Interestingly, nanoparticles from PPP₇₀-*b*-P3MT₁₁₅ and PPP₇₀-*b*-P3MT₁₈₀ showed multi-line morphology (mainly double-line) (Figure 2.7e-h)

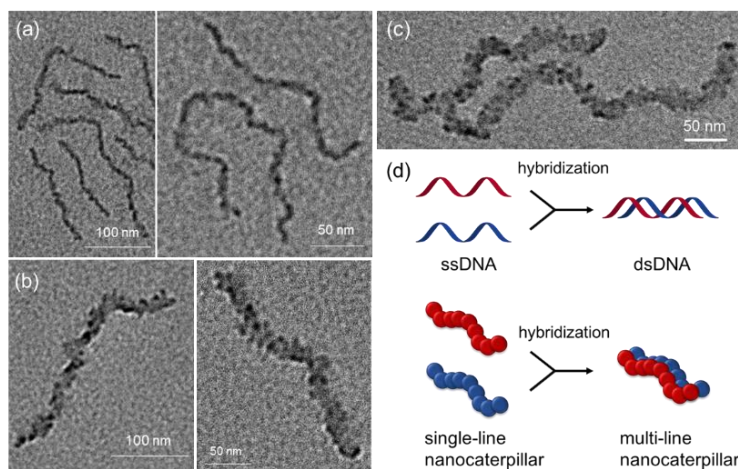
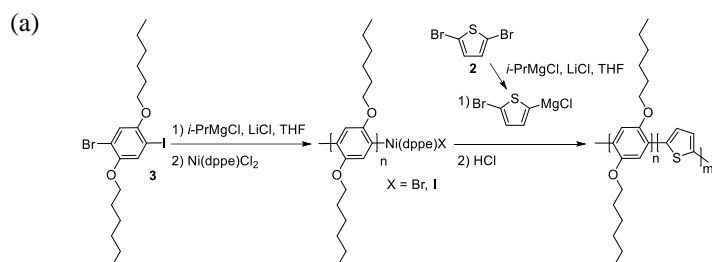


Figure 2.8. TEM images of the nanostructures from PPP-*b*-P3MTs on Cu/C TEM grid: (a) PPP₇₀-*b*-P3MT₅₀, (b) PPP₇₀-*b*-P3MT₁₁₅, and (c) PPP₇₀-*b*-P3MT₁₈₀. (d) Schematic comparison between the formation of double-stranded DNA (dsDNA) and multi-line nanocaterpillars.

TEM images of nanoparticles from PPP-*b*-P3MTs showed single to multi-line transformation of nanoparticles as increasing DP of P3MT (Figure 2.8). The nanospheres forming single to multi (mainly double)-line nanocaterpillar were

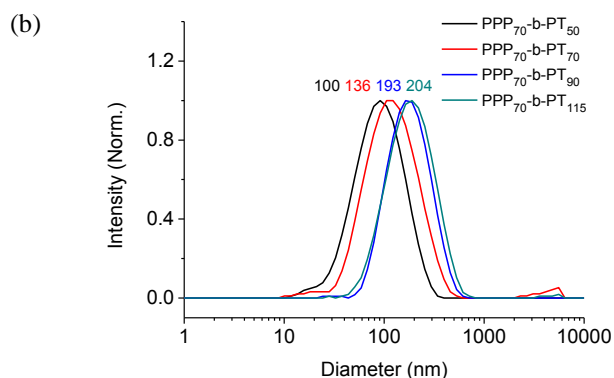
observed in TEM images as well (Figure 2.8). Compared to nanoparticles from PPP-*b*-PT which only formed single-line nanocaterpillar (Figure 2.9), nanoparticles from PPP-*b*-P3MT showed single to multi-line nanocaterpillars in TEM images (Figure 2.8)

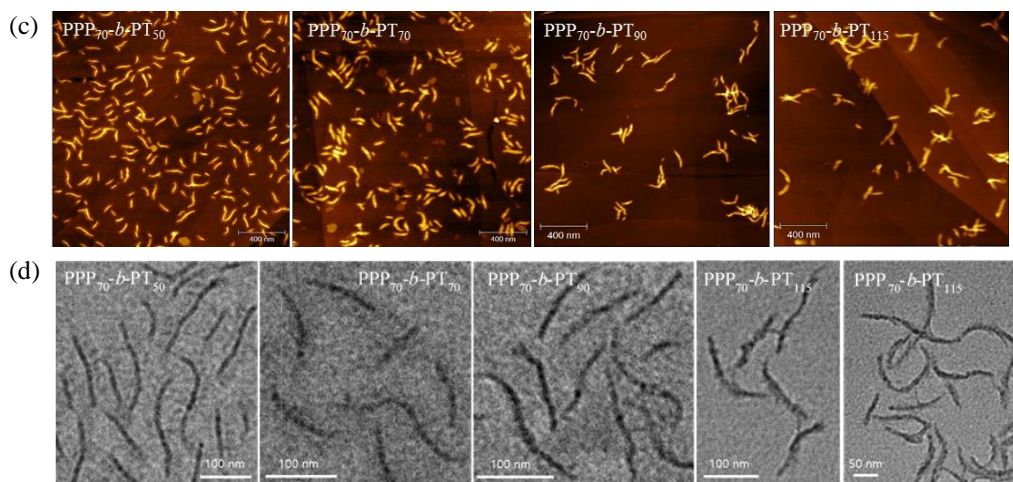


entry	Ni(dppe)Cl ₂ : 3 : 2	<i>M_n</i> (PDI) of PPP ^a	DP of PT ^b	yield
1	1 : 70 : 50	27.6k (1.08)	33	68%
2	1 : 70 : 70	26.0k (1.10)	41	70%
3	1 : 70 : 90	20.5k (1.05)	61	65%
4	1 : 70 : 115	19.8k (1.09)	99	67%

^aMeasured by THF SEC calibrated using polystyrene standards.

^bEstimated by gas chromatography-mass spectrometry.





	<i>PPP₇₀-b-PT₅₀</i>	<i>PPP₇₀-b-PT₇₀</i>	<i>PPP₇₀-b-PT₉₀</i>	<i>PPP₇₀-b-PT₁₁₅</i>
<i>L_n</i>	84 nm	94 nm	127 nm	131 nm
<i>L_w/L_n</i>	1.14	1.14	1.17	1.16
<i>Height</i> (<i>STDEV</i>)	4.4 nm (0.8 nm)	6.1 nm (0.8 nm)	7.3 nm (1.0 nm)	7.3 nm (0.8 nm)

Figure 2.9. (a) Synthetic results of PPP-*b*-PT by the GRIM method with monomer **2** and **3**. (b) DLS profiles of PPP-*b*-PT nanoparticles in chloroform at 20 °C. (c) AFM images of the nanostructures from PPP-*b*-PTs on HOPG. (d) TEM images of the nanostructures from PPP-*b*-PTs on Cu/C TEM grid.

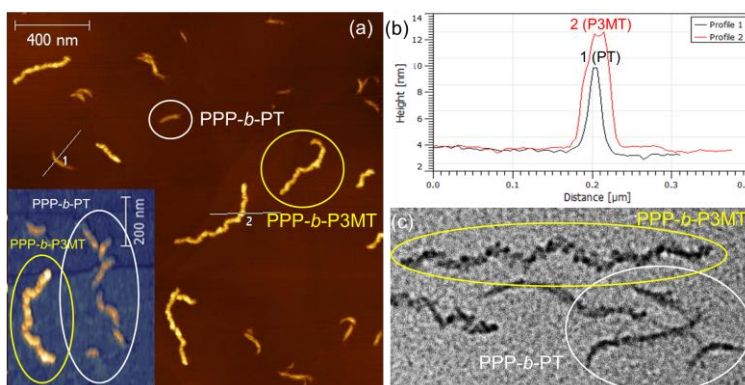
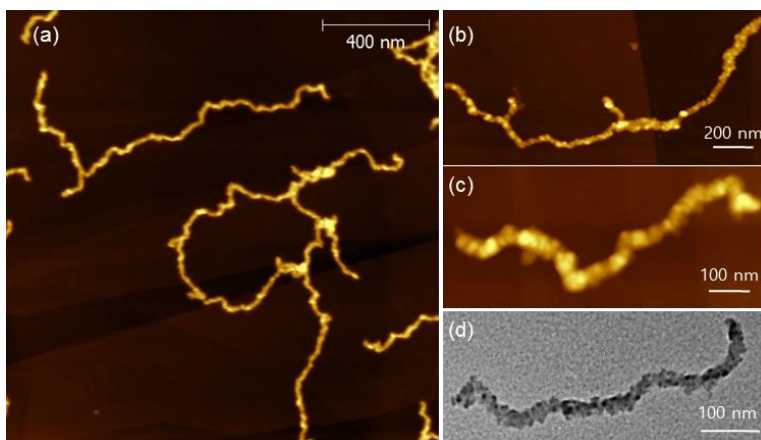


Figure 2.10. (a) AFM images, (b) height profiles and (c) TEM images obtained from the mixtures of nanostructures from $\text{PPP}_{70}\text{-}b\text{-P3MT}_{70}$ ($M_n = 18.3\text{k}$ and $\text{PDI} = 1.06$ of PPP, actual DP of P3MT = 65, $L_n = 315\text{ nm}$, $L_w/L_n = 1.34$) and $\text{PPP}_{70}\text{-}b\text{-PT}_{90}$ ($M_n = 20.5\text{k}$ and $\text{PDI} = 1.05$ of PPP, actual DP of PT = 61, $L_n = 127\text{ nm}$, $L_w/L_n = 1.17$).

To clearly demonstrate the difference between nanostructures from PPP-*b*-P3MT and PPP-*b*-PT, 1 to 1 mixture of nanoparticles from PPP-*b*-P3MT and PPP-*b*-PT were fabricated onto HOPG and Cu/C grid (Figure 2.10). AFM and TEM images of this mixture showed the clear difference between those two nanoparticles in a view of length, height, and multi-line morphology (Figure 2.10).



	PPP(EH) ₁₀₀ - <i>b</i> -P3MT ₅₀	PPP(EH) ₁₀₀ - <i>b</i> -P3MT ₉₀	PPP(EH) ₁₀₀ - <i>b</i> -P3MT ₁₃₀
L_n	179 nm	431 nm	n.d.
L_w/L_n	1.34	1.76	n.d.
<i>Height</i> (<i>STDEV</i>)	6.1 nm (0.7 nm)	7.8 nm (1.0 nm)	14.4 nm (2.3 nm)

Figure 2.11. AFM images of the nanostructures from PPP(EH)-*b*-P3MTs on HOPG: (a) PPP(EH)₁₀₀-*b*-P3MT₉₀, (b) PPP(EH)₁₀₀-*b*-P3MT₁₃₀. (c) High-resolution AFM images of the nanostructures from PPP(EH)₁₀₀-*b*-P3MT₁₃₀. (d) TEM images of the nanostructures from PPP(EH)₁₀₀-*b*-P3MT₁₃₀ on Cu/C TEM grid.

During the preparation of PPP-*b*-P3MT, we observed that solubility of PPP₇₀-*b*-P3MT₁₈₀ was marginal. To improve the solubility, 2-ethylhexyl side chain instead of *n*-hexyl side chain was introduced in PPP first block. Indeed, this side chain engineering improved solubility and elongation behaviour of nanoparticles (Figure 2.7 and Figure 2.11).

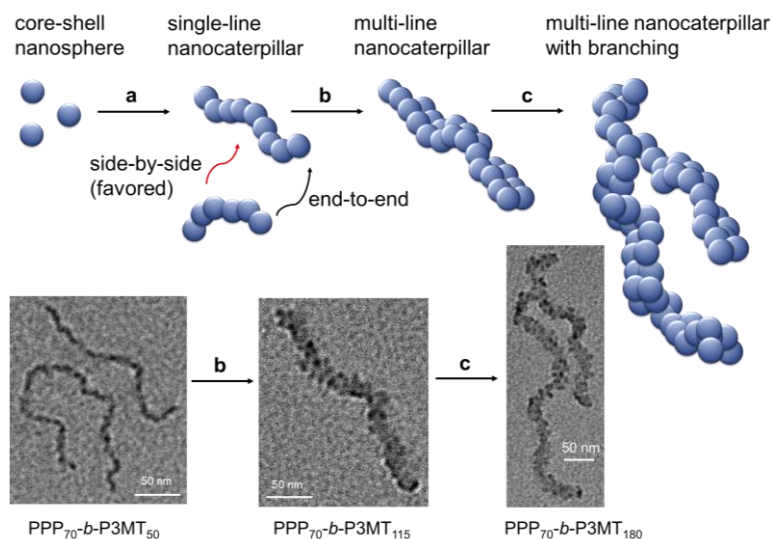


Figure 2.12. Proposed mechanism for the formation of the multi-line nanocaterpillars from PPP-*b*-P3MT

Based on all data we observed, the formation of multi-line nanocaterpillar structures was proposed (Figure 2.12). Firstly, nanospheres from PPP-*b*-P3MT evolved to single-line nanocaterpillars just like as previously suggested PPP-*b*-PT (Figure 2.5 and Figure 2.12a). As DP of P3MT increased, this single-line nanocaterpillars uniquely transformed to multi-line nanocaterpillars via side-by-side interaction (Figure 2.12b). This might be happen because the side-by-side attachment could minimize exposed area of core more than end-to-end attachment. Moreover, less chance to meet end-to-end fashion could affect to this phenomenon. Finally, as DP of P3MT increased more, some of core part was not shielded by shell effectively, thus long chain-branching occurred (Figure 2.12c).

Conclusion

In conclusion, unique hierarchical transformation of nanoparticles depending on DP of P3MT was achieved by in situ nanoparticlization of fully conjugated PPP-*b*-P3MT. The nanoparticles from PPP-*b*-P3MT formed nanospheres at early stage, and they evolved to single-line nanocaterpillars to multi-line nanocaterpillars, and finally to long-chain branched multi-line nanocaterpillars. This transformation of PPP-*b*-P3MT was quite different from that of PPP-*b*-PT only forming single-line nanocaterpillars. Overall, this study indicated the importance of core packing mode and solubility of nanoparticles.

Part III. In situ nanoparticlization of PPP first block with block and random copolymers of thiophene and (3-methylthiophene) as second block

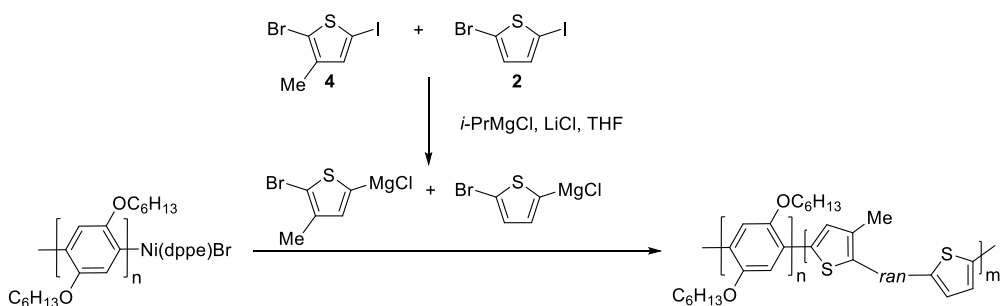
Introduction

We are now studying the effect of second block structures on in situ nanoparticlization of fully conjugated polymers. Two examples, i.e. PPP-*b*-PT⁴ and PPP-*b*-P3MT¹³, showed that packing mode and solubility of second block greatly affected to the resulting nanostructure. To further confirm and investigate these factors, we decided to synthesize the random copolymers of thiophene and (3-methylthiophene).

Results and Discussions

Table 2.3. Synthesis of PPP-*b*-P(3MT-*ran*-T) by the Grignard Metathesis

Polymerization Method



entry	feed ratio (Ni: 3 : 4 : 2)	1 st block SEC data ^a	P(3MT- <i>ran</i> -T) ^b	yield
1	1:70:65:30	$M_n = 11.6\text{k}$, PDI = 1.07	40- <i>ran</i> -21	46%
2	1:70:30:65	$M_n = 13.9\text{k}$, PDI = 1.06	16- <i>ran</i> -46	53%

^aMeasured by THF size exclusion chromatography calibrated using polystyrene standards.

^bEstimated by gas chromatography-mass spectrometry.

Two PPP-*b*-(P3MT-*ran*-T)s were prepared by the GRIM method by following the previously reported procedure (Table 2.3).⁹⁻¹⁰ The molecular weight of the first block PPP was controlled by fixing the [**3**]/[Ni(dppe)Cl₂] to 70 (Table 2.3). The total DP of random copolymer second block was targeted at 95, but the feeding ratio of monomer **2** and monomer **4** was varied from 30:65 to 65:30.

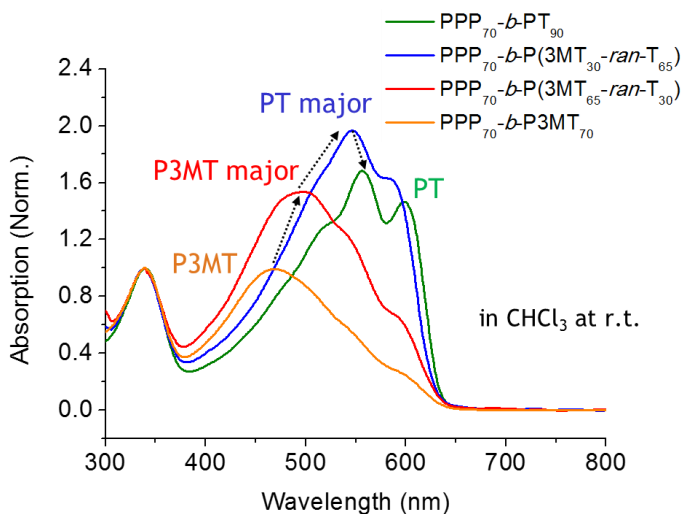


Figure 2.13. UV-vis spectra of PPP-*b*-P3MT, PPP-*b*-P(3MT-*ran*-T), and PPP-*b*-PT in chloroform at room temperature

UV-vis spectrum of the resulting polymers showed detail absorption of block copolymers. Briefly, the λ_{max} of diblock copolymers gradually red-shifted as the composition was changed from P3MT only to P(3MT-*ran*-T) to PT only (Figure 2.13). Moreover, the shape of vibronic peak was changed to become more distinct as increasing the portion of thiophene relative to 3-methylthiophene (Figure 2.13). It is noteworthy that UV-vis spectrum of PPP-*b*-P(3MT-*ran*-T) resembled that of PPP-*b*-P3MT when 3MT was the major portion of random copolymers (Figure 2.13). This means that the packing mode of PPP-*b*-P(3MT₆₅-*ran*-T₃₀) might be as similar as π -stacked packing observed in PPP-*b*-P3MT.

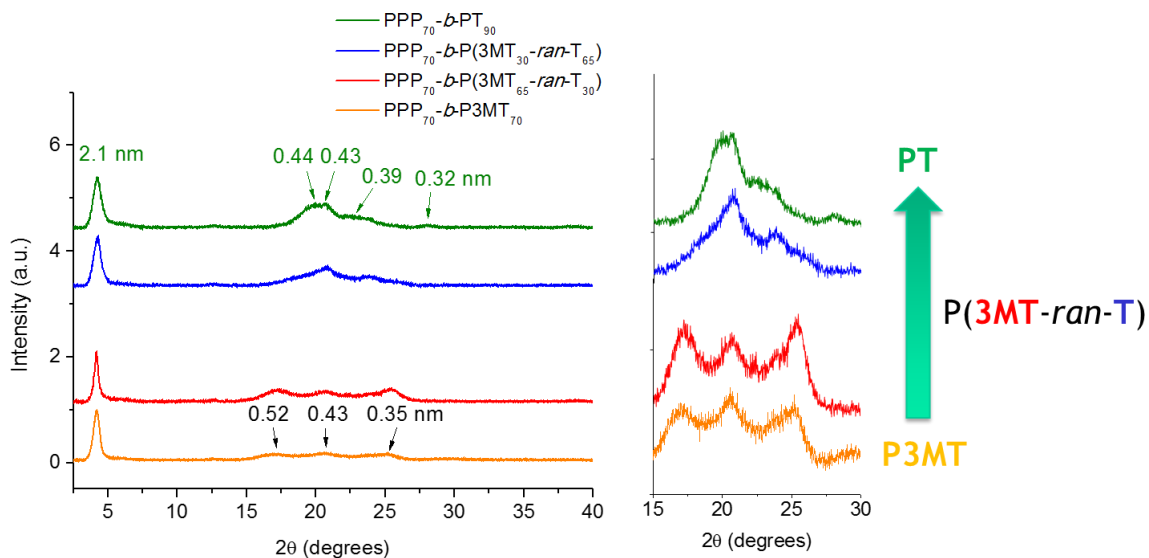


Figure 2.14. PXRD of PPP-*b*-P3MT, PPP-*b*-P(3MT-*ran*-T), and PPP-*b*-P3MTs

Investigation of the core structure of NPs from PPP-*b*-P(3MT-*ran*-T) performed with PXRD being compared to core structures both of PPP-*b*-P3MT and PPP-*b*-PT (Figure 2.14). Packing mode of PPP-*b*-P(3MT₆₅-*ran*-T₃₀) was π -stacked packing as similar as that of PPP-*b*-P3MT, whereas packing mode of PPP-*b*-P(3MT₃₀-*ran*-T₆₅) was resembling the herringbone packing mode of PPP-*b*-PT (Figure 2.14). This tendency for packing mode of PPP-*b*-P(3MT-*ran*-T) also matched with the absorption pattern in UV-vis spectrum (Figure 2.13).

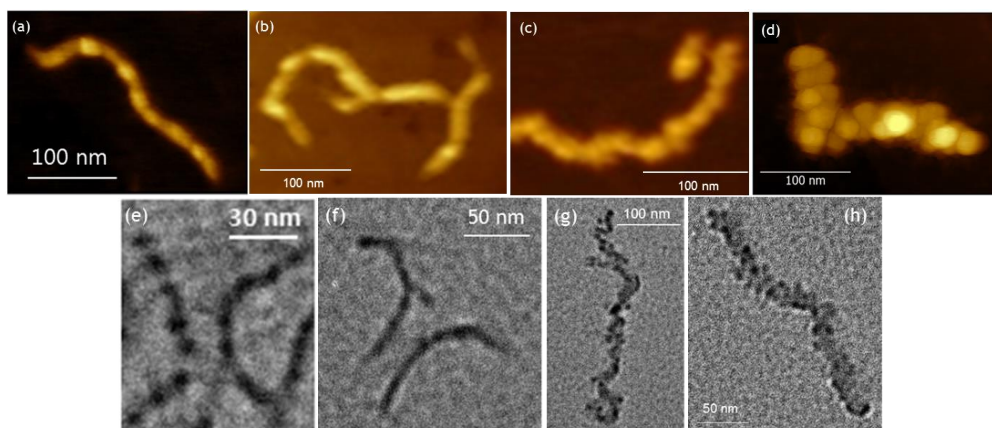


Figure 2.15. AFM images of the nanostructures from (a) PPP-*b*-PT, (b) PPP-*b*-P(3MT₃₀-*ran*-T₆₅), (c) PPP-*b*-P(3MT₆₅-*ran*-T₃₀), and (d) PPP-*b*-P3MT on HOPG. TEM images of the nanostructures from (e) PPP-*b*-PT, (f) PPP-*b*-P(3MT₃₀-*ran*-T₆₅), (g) PPP-*b*-P(3MT₆₅-*ran*-T₃₀), and (h) PPP-*b*-P3MT on Cu/C grid.

After getting the information about the core of NPs from UV-vis spectrum and PXRD, we performed AFM and TEM imaging to visualize real structure of nanoparticles and to find the relationship between core packing mode and the shape of nanostructures. Previously, we found that NPs from PPP-*b*-PT and PPP-*b*-P3MT were single-line nanocaterpillar and multi-line nanocaterpillar structures, respectively (Figure 2.15a,e for PPP-*b*-PT and Figure 2.15d,h for PPP-*b*-P3MT).^{4,13} For PPP-*b*-P(3MT-*ran*-T), PPP-*b*-P(3MT₃₀-*ran*-T₆₅) formed single-line nanocaterpillar, and PPP-*b*-P(3MT₆₅-*ran*-T₃₀) formed multi-line nanocaterpillar structures (Figure 2.15b,f for PPP-*b*-P(3MT₃₀-*ran*-T₆₅) and Figure 2.15c,g for PPP-*b*-P(3MT₆₅-*ran*-T₃₀)). Combining with the PXRD data, these AFM and TEM images revealed that core packing mode of the core-forming second block is an important factor to determine the final structure of NPs.

Conclusion

From the results from PPP-*b*-PT and PPP-*b*-P3MT, it was realized that core-packing mode of second block was highly important to determine nanostructures. In this case, we synthesized PPP-*b*-P(3MT-*ran*-T) block copolymers to examine the power of second block. Based on all data with UV-vis spectroscopy, PXRD, and AFM and TEM imaging of nanoparticles from PPP-*b*-P(3MT-*ran*-T)s, we further confirmed that the core-packing mode of second block was a highly important factor to determine the shape and size of resulting nanostructures.

References

- (1) Yoon, K.-Y.; Lee, I.-H.; Kim, K. O.; Jang, J.; Lee, E.; Choi, T.-L. *J. Am. Chem. Soc.* **2012**, *134*, 14291.
- (2) Kim, J.; Kang, E.-H.; Choi, T.-L. *ACS Macro Lett.* **2012**, *1*, 1090.
- (3) Lee, I.-H.; Amaladass, P.; Yoon, K.-Y.; Shin, S.; Kim, Y.-J.; Kim, I.; Lee, E.; Choi, T.-L. *J. Am. Chem. Soc.* **2013**, *135*, 17695.
- (4) Lee, I.-H.; Amaladass, P.; Choi, T.-L. *Chem. Commun.* **2014**, *50*, 7945.
- (5) Yoon, K.-Y.; Lee, I.-H.; Choi, T.-L. *RSC Adv.* **2014**, *4*, 49180.
- (6) Yoon, K.-Y.; Shin, S.; Kim, Y.-J.; Kim, I.; Lee, E.; Choi, T.-L. *Macromol. Rapid Commun.* **2015**, *36*, 1069.
- (7) Shin, S.; Yoon, K.-Y.; Choi, T.-L. *Macromolecules* **2015**, *48*, 1390.
- (8) Novak, B. M.; Risse, W.; Grubbs, R. H. *Adv. Polym. Sci.* **1992**, *102*, 47.

- (9) Miyakoshi, R.; Shimono, K.; Yokoyama, A.; Yokozawa, T. *J. Am. Chem. Soc.* **2006**, *128*, 16012.
- (10) Miyakoshi, R.; Yokoyama, A.; Yokozawa, T. *Chem. Lett.* **2008**, *37*, 1022.
- (11) Brown, P. J.; Thomas, D. S.; Köhler, A.; Wilson, J. S.; Kim, J.-S.; Ramsdale, C. M.; Siringhaus, H.; Friend, R. H. *Phys. Rev. B* **2003**, *67*, 064203.
- (12) Samitsu, S.; Shimomura, T.; Heike, S.; Hashizume, T.; Ito, K. *Macromolecules* **2008**, *41*, 8000.
- (13) Lee, I.-H.; Amaladass, P.; Choi, I.; Bergmann V. W.; Weber, S. A. L.; Choi, T.-L. *Polym. Chem.* **2016**, *Advance Article* (DOI:10.1039/C5PY01967B)
- (14) Mo, Z.; Lee, K.-B.; Moon, Y. B.; Kobayashi, M.; Heeger, A. J.; Wudl, F. *Macromolecules* **1985**, *18*, 1972.
- (15) Yamamoto, T.; Komarudin, D.; Arai, M.; Lee, B. L.; Suganuma, H.; Asakawa, N.; Inoue, Y.; Kubota, K.; Sasaki, S.; Fukuda, T.; Matsuda, H. *J. Am. Chem. Soc.* **1998**, *120*, 2047.
- (16) Tsuzuki, S.; Honda, K.; Azumi, R. *J. Am. Chem. Soc.* **2002**, *124*, 12200.

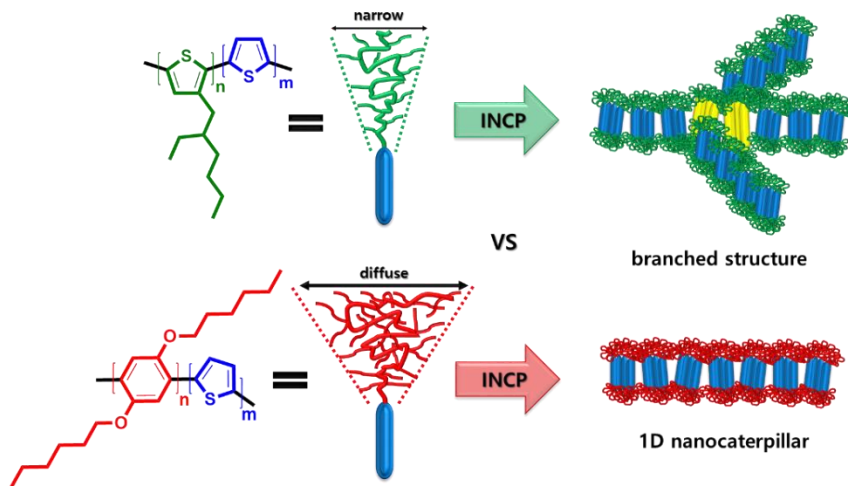
Chapter 3

In situ nanoparticlization of fully conjugated block copolymers using Grignard Metathesis method: Effect of shell block

Background

Fabrication of nanocaterpillar structures via in situ nanoparticlization of the fully conjugated diblock copolymer, i.e. poly(2,5-dihexyloxy-1,4-phenylene)-*block*-polythiophene (PPP-*b*-PT), catalyzed by Grignard Metathesis (GRIM) method, was successfully achieved.⁴ Moreover, much longer single- to multi-line nanocaterpillar structures were also successfully fabricated by in situ nanoparticlization of poly(2,5-dihexyloxy-1,4-phenylene)-*block*-poly(3-methylthiophene) (PPP-*b*-P3MT).⁸ One of the lessons from these two examples was that small molecular structural change of core block could make huge difference for in situ self-assembly process. In detail, we found that the impact of the additional methyl group introduced to polythiophene on the packing mode of second block and solubility of nanoparticles dramatically changed in situ self-assembly behavior of the corresponding diblock copolymers. Encouraged by this ‘butterfly effect’ of the structural modification on in situ nanoparticlization, in this time, we introduced poly(3-alkylthiophene) (P3AT) as the first block instead of PPP, whereas the second block was maintained as polythiophene.³ The main reason for the introduction of P3AT as the first block (shell) was its smaller hydrodynamic volume compared to PPP, providing highly exposed core during in situ nanoparticlization leading to multi-dimensional nanostructures (Scheme 3.1).³ Furthermore, poly(3-alkylthiophene) (P3AT) is even much well-known charge transporting material compared to PPP, which would expand the application of nanoparticles in optoelectronics. In this chapter, the in situ nanoparticlization of the fully conjugated P3AT-*b*-PT is described.

Scheme 3.1. In situ nanoparticlization of P3EHT-*b*-PT (highly exposed cores are depicted in yellow) and PPP-*b*-PT



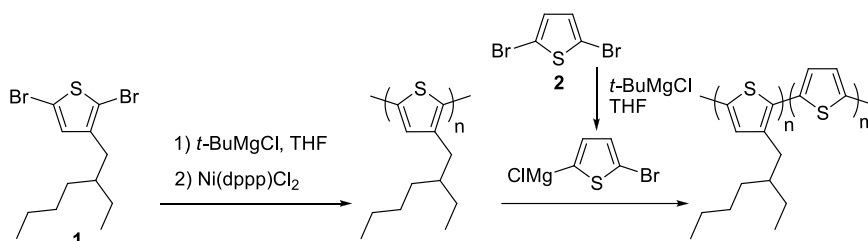
Part I. In situ nanoparticlization of poly(3-(2-ethylhexyl)thiophene)-*block*-polythiophene (P3EHT-*b*-PT)

Introduction

As an exemplary system, we choose P3EHT as the first block with PT as the second block. P3EHT was selected as the first block, because not only the controlled synthesis of P3EHT is possible by GRIM method,⁹ but also its high solubility originated from branched 2-ethylhexyl side chain could increase the solubility of the resulting diblock copolymer or nanoparticles (NPs) in reaction solvent, i.e. THF. PT was chosen as the second block to make the comparison with PPP-*b*-PT easy and to induce the in situ self-assembly of P3EHT-*b*-PT.

Results and Discussions

Table 3.1. Synthesis of P3EHT-*b*-PT by GRIM method



entry	[Ni cat.]:[1]:[2]	M_n (PDI) of P3EHT ^a	DP of PT ^b	yield
1	1:100:33	9.3k (1.25)	27	40%
2	1:100:67	9.9k (1.23)	58	44%
3	1:100:100	12.4k (1.23)	80	50%

^a Determined by THF SEC calibrated using PS standards. M_n is given in g/mol.

^b Estimated by GC-MS.

Synthesis of fully conjugated polythiophene diblock copolymers was achieved via the quasi-living Grignard metathesis (GRIM) method.⁹ Fixing catalyst ((1,3-*bis*(diphenylphosphino)propane)dichloronickel (II) (Ni(dppp)Cl₂)) loading as 1 mol% with respect to monomer **1**, three different samples with various feed ratios of **1** to **2**, such as 100:33, 100:67, and 100:100, were prepared (Table 3.1). The number average molecular weight (M_n) and polydispersity index (PDI) of the P3EHT first block for all three samples were approximately 10 kg/mol and 1.2, respectively, suggesting that GRIM was well-controlled (Table 3.1, entries 1-3). The degree of polymerization (DP) of the second PT block was estimated using gas chromatography-mass spectrometry (GC-MS), and the DP of PT increased linearly

with an increase in the equivalent of **2** (Table 3.1, entries 1-3). All three nanoparticles from P3EHT-*b*-PT were soluble and stable in common organic solvents such as THF, chloroform, toluene, and chlorobenzene.

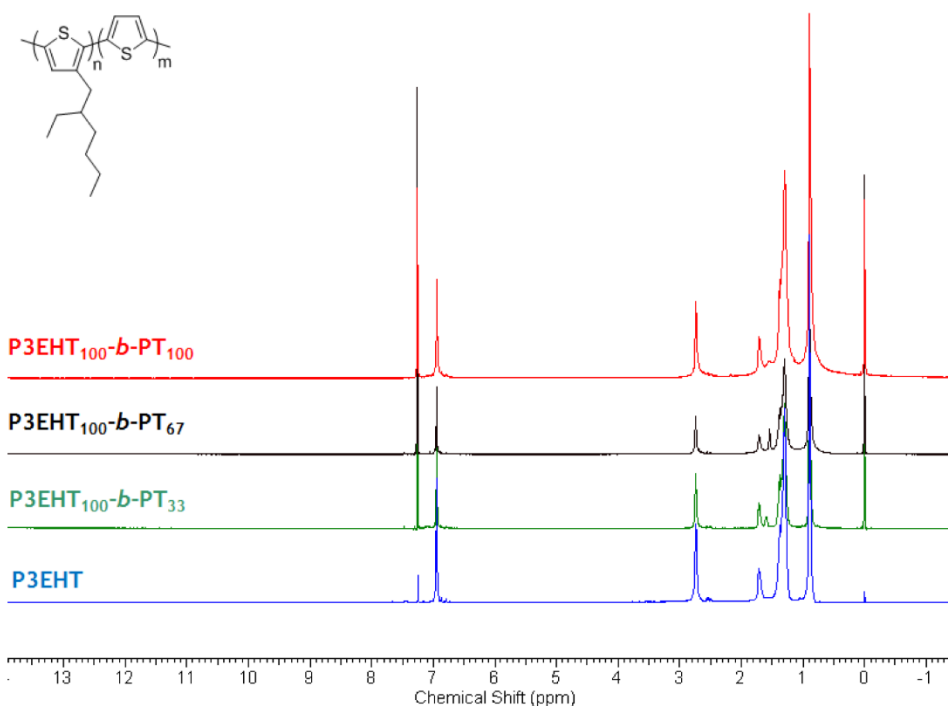


Figure 3.1. ^1H NMR spectra of P3EHT and P3EHT-*b*-PT in CDCl_3

At first, ^1H NMR spectroscopy of P3EHT-*b*-PT was checked in CDCl_3 . Interestingly, ^1H NMR spectra of P3EHT homopolymer and P3EHT-*b*-PT were identical (Figure 3.1). There are two possible explanations. One is that P3EHT-*b*-PT was not synthesized, and only P3EHT homopolymer was formed. Second is that P3EHT-*b*-PT formed core-shell type nanostructures. In this case, PT formed core part

which was not solvated in CDCl_3 at all. From the examples of other previous INCP, we expected that later case might work.¹⁻⁸ However, to verify this argument clearly, we investigated UV-vis spectroscopy (Figure 3.2).

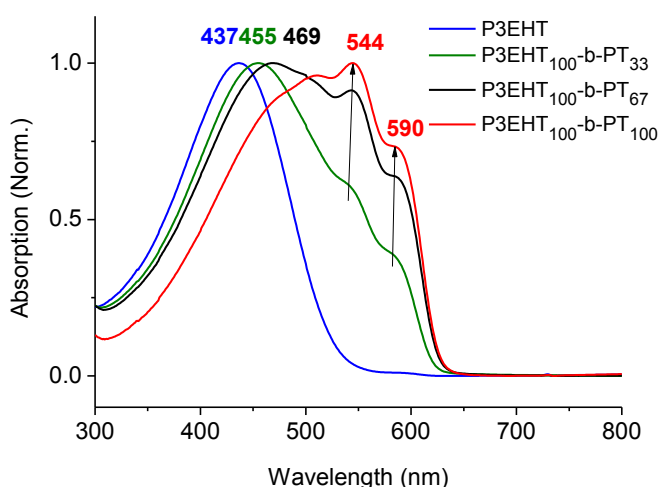


Figure 3.2. UV/vis spectra of nanostructures from P3EHT-*b*-PT in toluene at room temperature

P3EHT and P3EHT-*b*-PT were analyzed by UV-vis spectroscopy in toluene at room temperature. It is notable that absorption of PT was clearly observed, meaning the successful block copolymerization and core-shell type nanoparticle formation (Figure 3.1 and Figure 3.2). Compared to absorption of P3EHT, λ_{max} and onset point of P3EHT-*b*-PT red-shifted from 437 to 544 nm and from 2.4 to 2.0 eV, respectively (Figure 3.2). Moreover, P3EHT-*b*-PT showed vibronic peak at 544 and 590 nm even in solution state. This vibronic peak intensity as well as red-shift of λ_{max} and onset point became enhanced as increasing DP of PT (Figure 3.2).

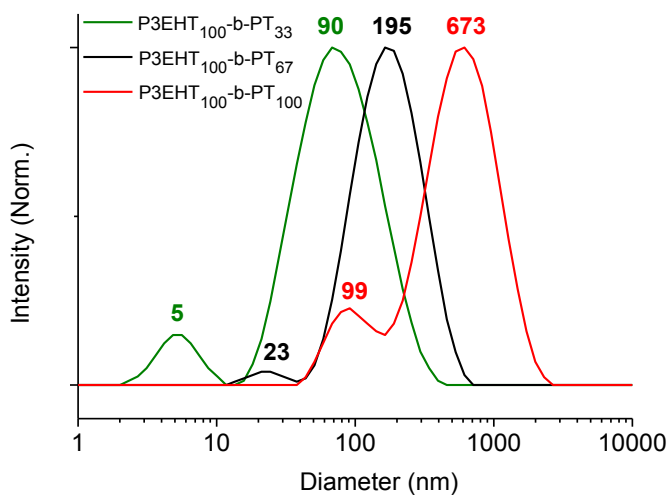


Figure 3.3. DLS profiles of nanostructures from P3EHT-*b*-PT in toluene

After observing the change of optical properties for diblock copolymers depending on DP of PT, we investigated the size of nanoparticles in toluene using dynamic light scattering (DLS). The size of nanoparticles changed from 90 to 195 to 673 nm as increasing DP of PT from 27 to 58 to 80 (Figure 3.3).

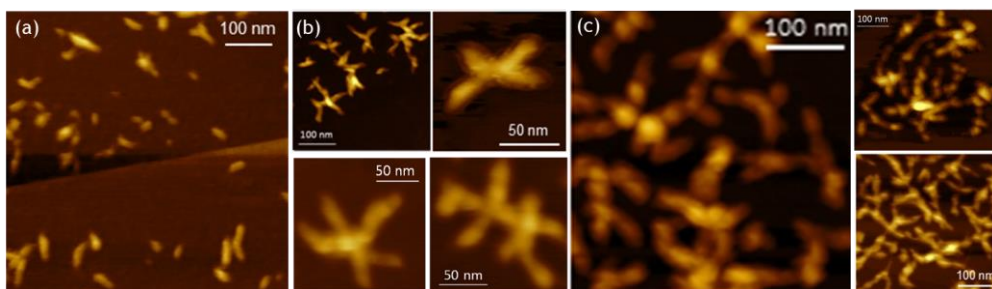


Figure 3.4. AFM images of nanostructures from (a) P3EHT₁₀₀-*b*-PT₃₃, (b) P3EHT₁₀₀-*b*-PT₆₇, and (c) P3EHT₁₀₀-*b*-PT₁₀₀

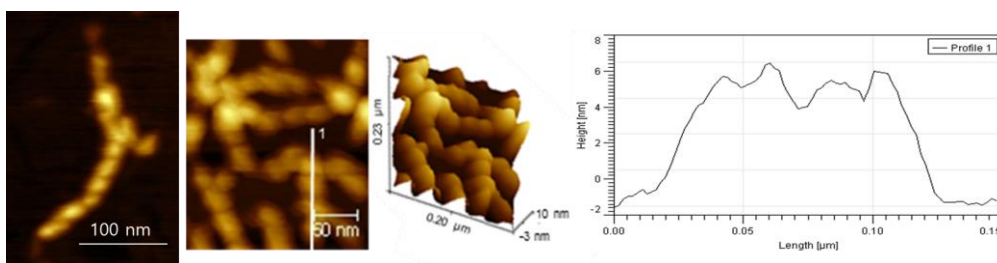


Figure 3.5. High resolution AFM images of nanostructures from P3EHT-*b*-PT with side-view and cross-sectional profile

With information for optical property and size of nanoparticles in hand, we started to identify the structure of nanoparticles from P3EHT-*b*-PT using atomic force microscopy (AFM) and transmission electron microscopy (TEM) analyses. For the AFM imaging, highly ordered pyrolytic graphite (HOPG) was chosen. The AFM images obtained from mica surface only showed highly aggregated large micron-sized nanoparticles, which might be caused by secondary interaction between nonpolar sample and polar surface. The AFM images on HOPG revealed that the nanoparticles from P3EHT-*b*-PT evolved according to DP increase (Figure 3.4). Specifically, P3EHT₁₀₀-*b*-PT₃₃ formed nanorod structures, which size is near to 50-100 nm (Figure 3.4). Next, P3EHT₁₀₀-*b*-PT₆₇ formed nanostar (nanorod with branching) structures, and P3EHT₁₀₀-*b*-PT₁₀₀ finally formed nanonetwork (highly branched and linked nanostar) structures (Figure 3.4). Moreover, the height of nanostructures gradually increased from 1-8 nm as increasing DP of PT, suggesting the core expansion might be related with structural evolution. It is interesting that high resolution AFM images showed highly undulated nanostructures (Figure 3.5).

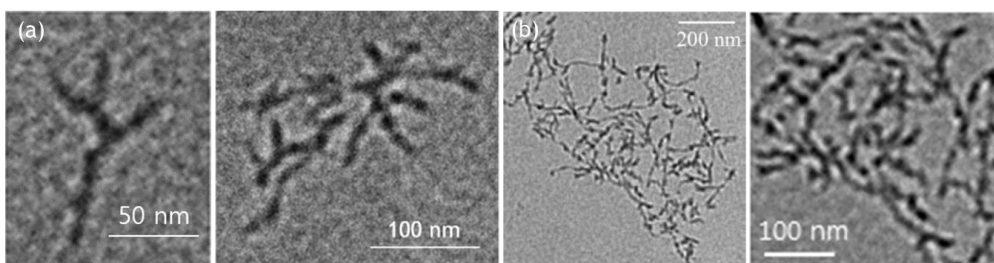


Figure 3.6. TEM images of nanostructures from (a) P3EHT₁₀₀-*b*-PT₆₇ and (b) P3EHT₁₀₀-*b*-PT₁₀₀

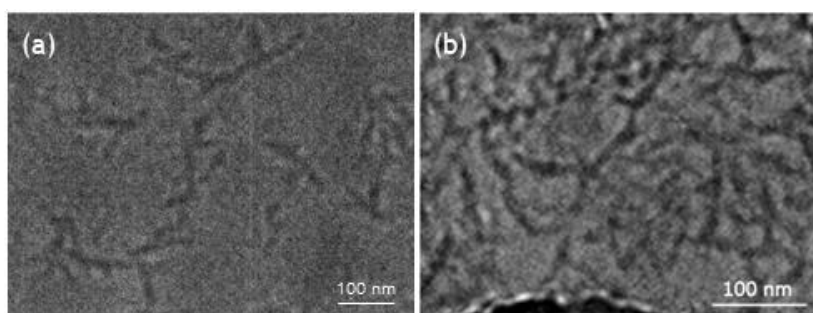


Figure 3.7. *Cryo*-TEM images of nanostructures from (a) P3EHT₁₀₀-*b*-PT₆₇ and (b) P3EHT₁₀₀-*b*-PT₁₀₀ in CHCl₃

TEM images of nanoparticles from P3EHT-*b*-PTs showed the same structural evolution observed in AFM imaging (Figure 3.4 and Figure 3.6). In particular, high-resolution of TEM images showed that nanospheres were aligned with minimal contact (Figure 3.6), which might be related with the undulation of nanoparticles observed in AFM (Figure 3.5). Significantly, *cryo*-TEM imaging of nanostructures from P3EHT-*b*-PTs showed nanostar and nanonetwork structures (Figure 3.7). This demonstrate that nanoparticles observed in dry-AFM and TEM images were real, and there was no secondary interaction between sample and HOPG surface (or Cu/C grid).

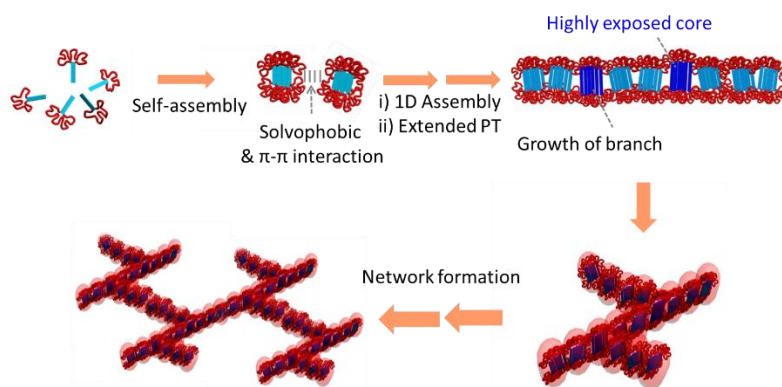


Figure 3.8. Proposed mechanism for the formation of the branched nanoparticles from P3EHT-*b*-PT.

Based on previous observations, the formation of nanoparticles from P3EHT-*b*-PT was proposed (Figure 3.8). At first, P3EHT-*b*-PT formed nanospheres due to high solvophobicity of second block (Figure 3.8). As the reaction goes on during the self-assembly process, the core of nanoparticles exposed to solvent (Figure 3.8). To minimize this unfavorable situation, the exposed core of nanoparticles clung to each other (Figure 3.8). However, some part of core was highly exposed, thus shell could not cover the core effectively. This highly exposed core became branching point forming nanostar, and as this process became severe, finally highly branched nanonetwork was formed (Figure 3.8).

Finally, it is noteworthy that the resulting nanostructures were stable under external stimuli such as high temperature up to 80 °C in toluene and sonication.

Conclusion

In summary, we fabricated nanoparticles from fully conjugated P3EHT-*b*-PT. These nanoparticles were formed during the GRIM polymerization of P3EHT-*b*-PT in single-step. The shape of nanoparticles easily tuned by simply changing the DP of PT, and nanoparticles were evolved from nanosphere to nanostar, finally to nanonetworks. Moreover, obtained nanoparticles were highly stable under external stimuli such as high temperature and sonication. We believed that this INCP process and newly generated nanoparticles will be useful for future nanoparticle formation and optoelectronic application.

Part II. In situ nanoparticlization of poly(3-(2-octyldodecyl)thiophene)-*block*-polythiophene (P3ODT-*b*-PT)

Introduction

In situ nanoparticlization of P3EHT-*b*-PT successfully fabricated short nanorod to branched nanoparticles such as nanostar and nanonetwork.³ However, even the DP of PT increased up to 80, the solubility of resulting NPs were poor and the resulting NPs were branched with less control. Thus, to improve the solubility of NPs and to reduce the number of branching at high DP of PT, P3ODT instead of P3EHT was introduced as first block. P3ODT has long and branched 2-octyldodecyl chains increasing hydrodynamic volume of first block as well as solubility, which would allow for the formation of 1D nanostructures just like PPP-*b*-PT⁴ (Scheme 3.2).

Results and Discussions

Scheme 3.2. Comparison between in situ nanoparticlization of P3EHT-*b*-PT and P3ODT-*b*-PT

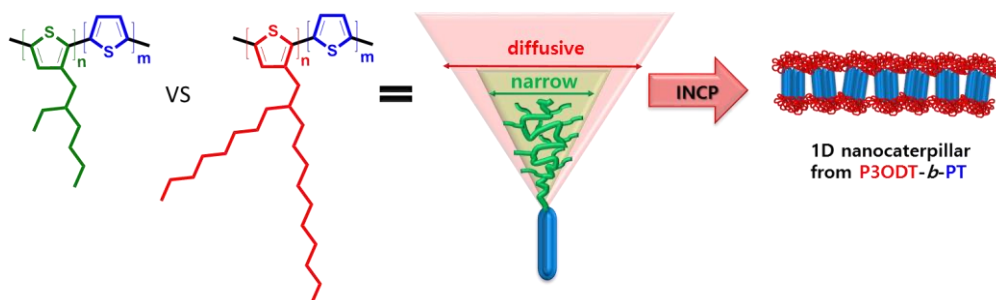
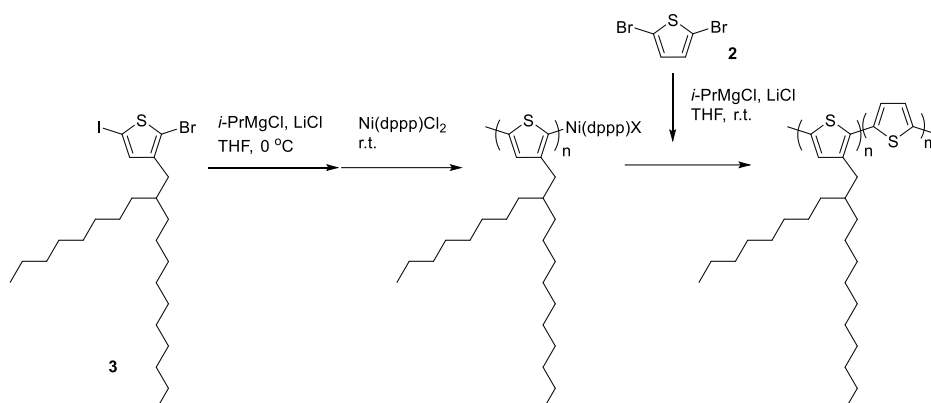


Table 3.2. Synthesis of P3ODT-*b*-PT by GRIM method



entry	Ni(dppp)Cl ₂ : 3 : 2	M_n (PDI) of P3ODT ^a	DP of PT ^b	yield	size ^c
1	1 : 50 : 50	M_n = 12.7k (1.07)	38	n.d.	61 nm
2	1 : 50 : 100	M_n = 13.2k (1.08)	89	76%	121 nm
3	1 : 50 : 150	M_n = 9.8k (1.09)	137	72%	207 nm

^a Determined by THF SEC calibrated using PS standards. M_n is given in g/mol.

^b Estimated by GC-MS.

^c Determined by DLS in chloroform at 20 °C

P3ODT-*b*-PTs were synthesized by GRIM method.⁹ Compared to the synthesis of P3EHT-*b*-PT, in this time, 2-bromo-5-iodo-3-(2-octyldodecylthiophene) (**3**) with LiCl was used to get better control over molecular weight, PDI, and yield (Table 3.2). The M_n and PDI of P3ODT were highly controlled, and DP of PT linearly increased from 38 to 137 as increasing the ratio of [**2**] to [Ni cat.] from 50 to 150. It is noteworthy that high solubility of P3ODT enabled the synthesis of P3ODT-*b*-PT with very high DP of PT up to 137. Previously, the maximum DP of PT for P3EHT-*b*-PT was limited to 80 due to the solubility limit.

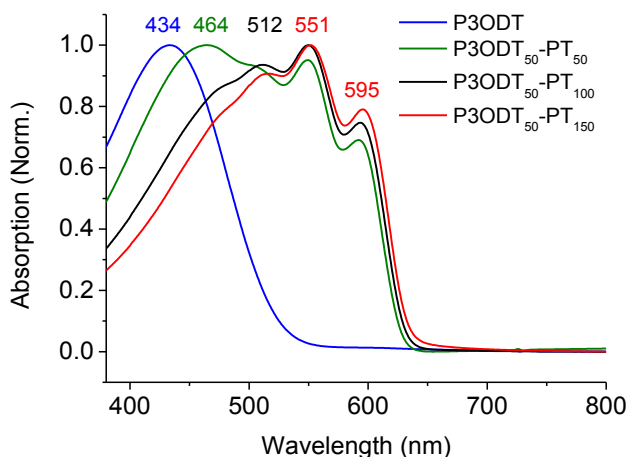


Figure 3.9. UV/vis spectra of nanostructures from P3ODT-*b*-PT in chloroform at room temperature

UV-vis spectrum of P3ODT-*b*-PT showed similar characteristics in comparison with that of P3EHT-*b*-PT. First, λ_{max} value in the UV-vis spectra was red-shifted from 434 to 551 nm as increasing the DP of PT from 0 to 137 (Figure 3.9). Moreover, vibronic peaks were enhanced as increasing DP of PT (Figure 3.9). Existence of vibronic peak is an indicative of strong π - π stacking of PT even in chloroform.¹¹⁻¹²

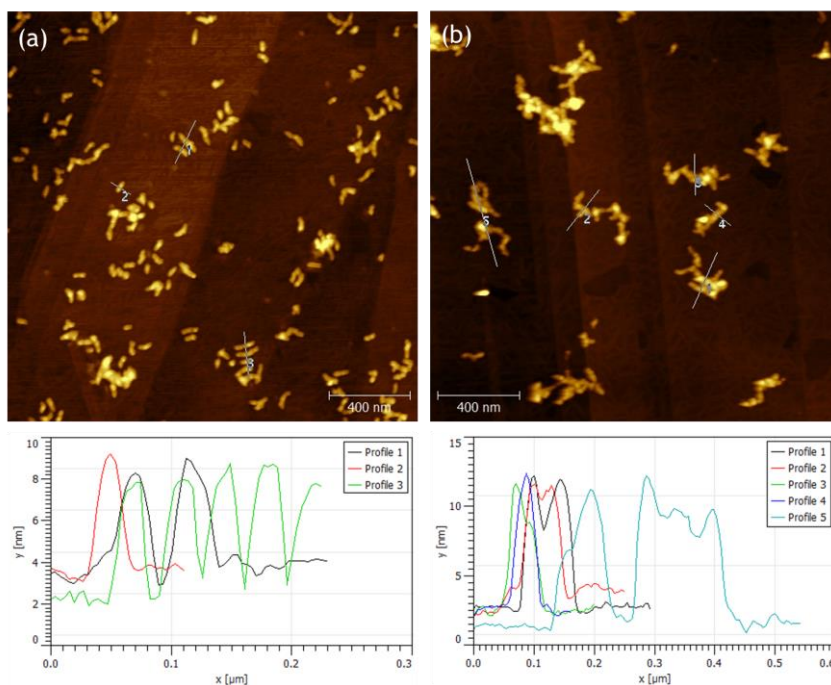


Figure 3.10. AFM images of nanostructures from (a) P3ODT₅₀-*b*-PT₁₀₀ and (b) P3ODT₅₀-*b*-PT₁₅₀

Next, the obtained nanostructures were characterized with DLS and AFM. The size of nanoparticles increased from 61 to 207 nm as increasing the DP of PT from 38 to 137 (Table 3.2). Compared to the size of NPs from P3EHT-*b*-PT (90–673 nm), size of NPs from P3ODT-*b*-PT was at most 200nm even at high DP of PT, 137 (Figure 3.3 and Table 3.2). AFM images of nanostructures from P3ODT₅₀-*b*-PT₁₀₀ and P3ODT₅₀-*b*-PT₁₅₀ showed 1D nanocaterpillars which length is near to 100 nm and slightly larger but branched nanoparticles, respectively (Figure 3.10). The size of NPs shown in AFM images were quite well-matched with the size of NPs obtained with DLS measurement in chloroform at 20 °C (Figure 3.10 and Table 3.2). NPs from

P3ODT₅₀-*b*-PT₁₀₀ exclusively formed 1D nanorod structures even NPs accommodated high DP of PT (89), but the length of NPs was still limited to 100 nm (Figure 3.10). Even though P3ODT was a good candidate to prohibit the highly exposed core to afford 1D nanorod structures, too much shielding could also prohibit the normal core exposure from the NPs during the polymerization, limiting the growth of nanoparticles toward long nanorod. Moreover, in case of P3ODT₅₀-*b*-PT₁₅₀, too large DP of PT (137) ultimately caused the highly exposed core, hampering the 1D growth, rather leading to branched nanoparticles (Figure 3.10). In case of in situ nanoparticlization of PPP-*b*-P3MT, the core expansion of NPs induced multi-line nanocaterpillar and long-chain branches;⁸ however, in this P3ODT-*b*-PT case, the transformation like PPP-*b*-P3MT was limited, and just afforded NPs obtained by irregular attachment of nanorods.

Conclusion

In summary, fully conjugated P3ODT-*b*-PTs with various DP of PT were successfully synthesized via the GRIM method, which spontaneously formed highly stable nanoparticles via INCP. Significantly, even at high DP of PT near 100, the 1D NPs were still obtained, which are the first example for the fabrication of 1D NPs from the fully conjugated polythiophene block copolymers with DP of PT over 50. We believe that this interesting NPs was able to be obtained by the aid of the large hydrodynamic volume of first block, P3ODT.

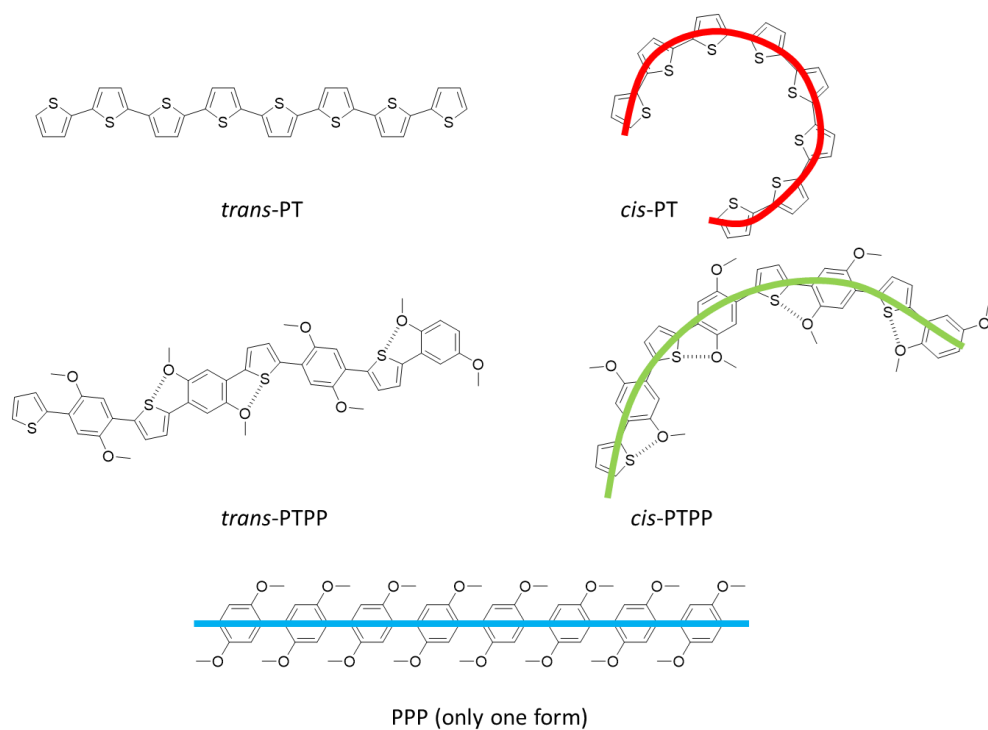
Part III. In situ nanoparticlization of poly(thiophene-*alt*-(*para*-phenylene))-*block*-polythiophene (PTPP-*b*-PT)

Introduction

Previously, we investigated the effect of hydrodynamic volume of first block on in situ self-assembly process (Schemes 3.1 and Scheme 3.2). There might be many reasons affecting to hydrodynamic volume such as dihedral angle, bulkiness and number of side chain, and isomers of backbone. In particular, we focused on the role of isomer form of first block for in situ self-assembly. As shown in Scheme 3.3, polythiophene and poly(thiophene-*alt*-(*para*-phenylene)) could have two *cis*- and *trans*- isomer forms in solution state, whereas poly(*p*-phenylene) has one possible form only. Even though, the equilibrium of *cis*- and *trans*- state in solution might be affected by the factors such as solvent and sort of side chains, we assumed that the linearity order of polymer backbone might be PPP>PTPP>PT (Scheme 3.3), because in situ nanoparticlization occurred in the same solvent, i.e. THF, thus deviation by solvent effect on polymer backbone structure might be minimal. Moreover, PT has the largest angle between repeat units in *cis*-form than PTPP (Scheme 3.3), again suggesting the linearity order of backbone as PPP>PTPP>PT. In this part, we suggest the relationship between the linearity of first block and the shape of resulting nanostructures.

Results and Discussions

Scheme 3.3. Possible *trans*- and *cis*-forms of PT, PTPP, and PPP. Note that PPP has only one form.



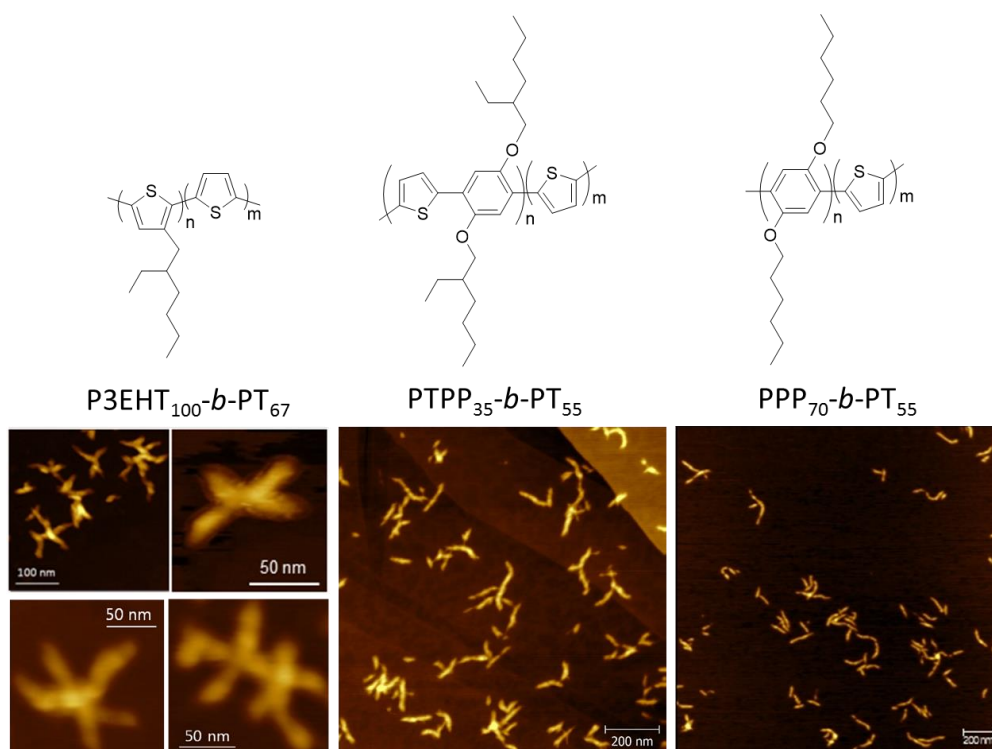


Figure 3.11. Comparison of the structure of P3EHT-*b*-PT, PTPP-*b*-PT, and PPP-*b*-PT. AFM images of each block copolymers are presented below the block copolymer structures.

Previously, in situ nanoparticlization of P3EHT-*b*-PT and PPP-*b*-PT formed the branched nanostructures and linear 1D nanocaterpillars.^{4,8} The NPs formed by in situ nanoparticlization of PTPP-*b*-PT was curious, because PTPP has the comparable number of side chains compared to that of P3EHT-*b*-PT, and their backbone is more rigid than P3EHT (Scheme 3.3). In contrast to the branched structures from P3EHT₁₀₀-*b*-PT₆₇,⁴ AFM images of PTPP revealed that PTPP₃₅-*b*-PT₅₅ formed exclusively 1D nanocaterpillar structures resembling 1D nanocaterpillars from PPP₇₀-

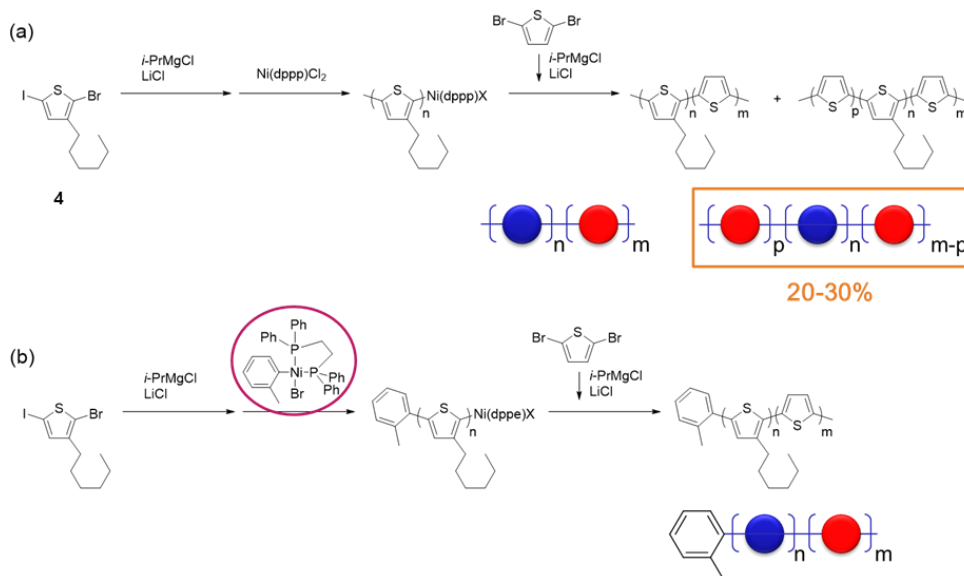
b-PT₅₅. This observation indicated that the importance of the backbone rigidity for in situ nanoparticlization, which might be related with the hydrodynamic volume of shell.

Part IV. In situ nanoparticlization of poly(3-hexylthiophene)-*block*-polythiophene (P3HT-*b*-PT) using externally initiating precatalyst

Introduction

Mechanistic investigation for GRIM polymerization has been reported, and revealed that the actual growing mechanism of polymer was bidirectional growth.¹³ The bidirectional growth caused the tail to tail defect inside the P3AT homopolymer chain.¹³ For block copolymerization, this bidirectional growth was still allowed leading to the mixture of diblock copolymer and triblock copolymer.¹⁴ Thus, to obtain well-defined diblock copolymer only, externally initiated precatalyst was introduced.¹⁴ Moreover, even though the amount of triblock copolymer relative to diblock copolymer was expected as small, this small contaminant would affect to in situ nanoparticlization process. Thus, in situ nanoparticlization of well-defined diblock copolymers and the mixture of diblock and triblock copolymers was investigated.

**Scheme 3.4. Synthesis of P3HT-*b*-PT by GRIM method using: (a) Ni(dppp)Cl₂,
(b) *o*-Tol-Ni(dppp)Br**



As a model system for investigation, P3HT-*b*-PT was selected. P3HT-*b*-PT was initially synthesized by GRIM method using conventional Ni(dppp)Cl₂ catalyst, and this block copolymerization might generate 20-30% of PT-*b*-P3HT-*b*-PT triblock copolymers based on the formula suggested by previous literatures (Scheme 3.4).¹³⁻
¹⁴ In contrast to Ni(dppp)Cl₂ catalyzed polymerization, *o*-TolNi(dppp)Br catalyzed polymerization only formed well-defined P3HT-*b*-PT without any contamination by triblock copolymers, because one side of polymer chain was blocked by *o*-Tol group promoting uni-directional growth of polymer chain (Scheme 3.4).

Table 3.3. Synthesis of P3HT₅₀-*b*-PT₄₀ and *o*Tol-P3HT₅₀-*b*-PT₄₀ by GRIM method

entry	catalyst	[Ni cat.]:[4]:[2]	<i>M_n</i> (PDI) of first block	DP of PT ^b	yield
1	Ni(dppp)Cl ₂	1:50:40	10.1k (1.23)	31	66%
2	<i>o</i> -TolNi(dppe)Br	1:50:40	10.4k (1.09)	29	64%

^a Determined by THF SEC calibrated using PS standards. *M_n* is given in g/mol.

^b Estimated by GC-MS.

Initially, P3HT₅₀-*b*-PT₄₀ was synthesized by GRIM polymerization using Ni(dppp)Cl₂ or *o*-TolNi(dppe)Br (Table 3.3). Two samples have been synthesized as comparable to each other. For example, molecular weight of P3HT, DP of PT, and yield of the resulting block copolymer were almost matched with each other (Table 3.3).

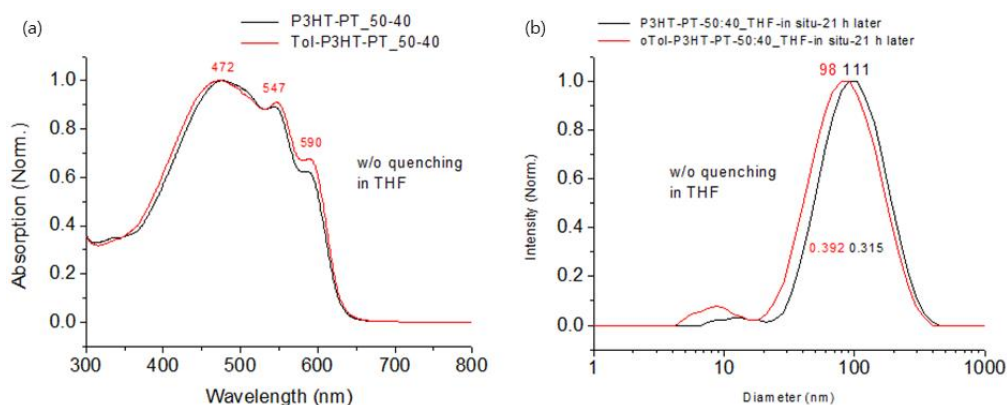


Figure 3.12. (a) UV-vis spectra and (b) DLS profiles of P3HT₅₀-*b*-PT₄₀ and *o*-Tol-P3HT₅₀-*b*-PT₄₀

The synthetic control was also confirmed by UV-vis spectroscopy .NPs from P3HT₅₀-*b*-PT₄₀ and *o*-Tol-P3HT₅₀-*b*-PT₄₀ showed almost matched UV-vis spectroscopy (Figure 3.12a). The size of NPs P3HT₅₀-*b*-PT₄₀ and *o*-Tol-P3HT₅₀-*b*-PT₄₀ were as similar as each other near to 100 nm (Figure 3.12b).

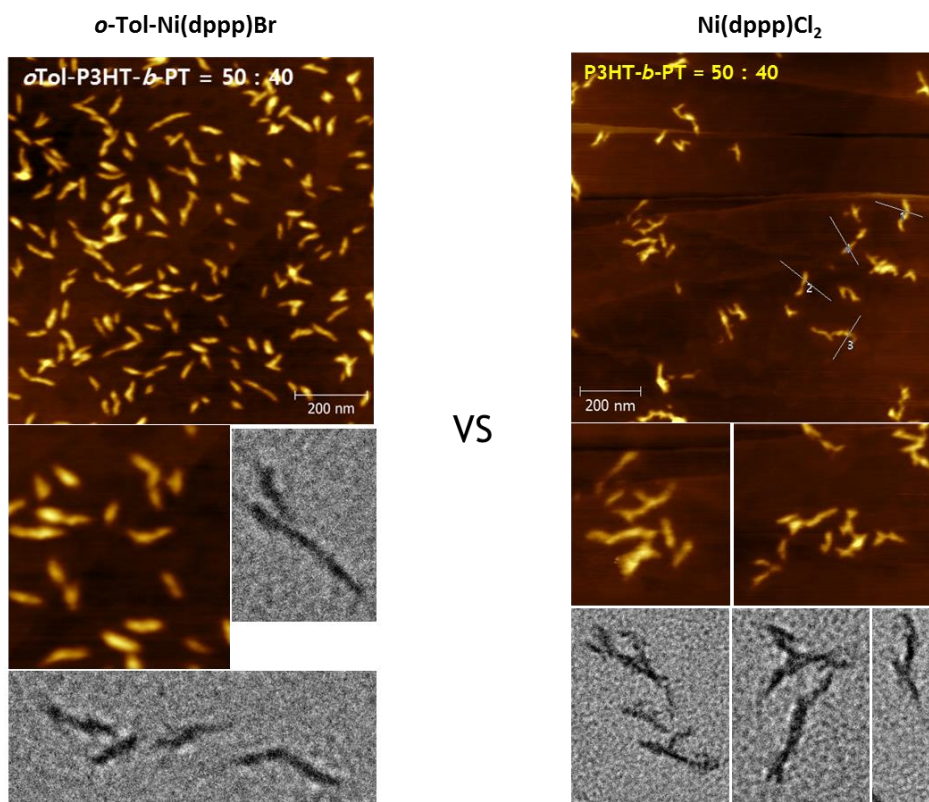


Figure 3.13. AFM and TEM images of NPs from *o*-Tol-P3HT₅₀-*b*-PT₄₀ (left) and P3HT₅₀-*b*-PT₄₀ (right)

The actual shape of NPs were visualized by AFM and TEM imaging techniques. AFM and TEM images of NPs from P3HT₅₀-*b*-PT₄₀ showed linear nanoparticles but close look on nanostructure exhibited ill-defined 1D nanorod

sometimes with branching (Figure 3.13). In contrast to the nanostructures from P3HT₅₀-*b*-PT₄₀, AFM and TEM images of NPs from *o*-Tol-P3HT₅₀-*b*-PT₄₀ revealed exclusive formation of 1D nanorod structures (Figure 3.13).

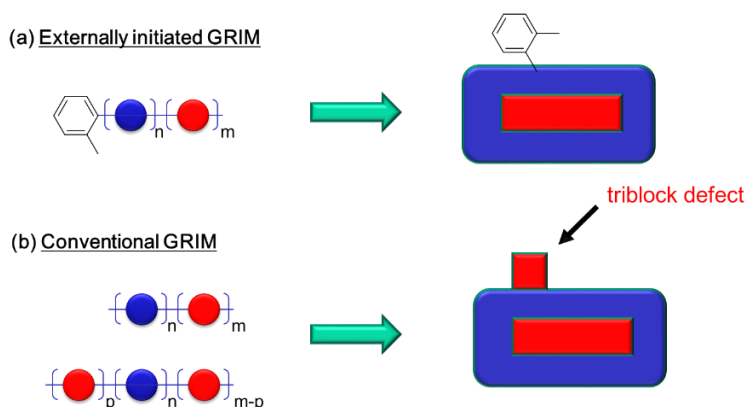


Figure 3.14. Proposed model for in situ nanoparticlization of (a) *o*-Tol-P3HT₅₀-*b*-PT₄₀ and (b) P3HT₅₀-*b*-PT₄₀

Based on all data described until now, we suggested the role of triblock defect. Initially, diblock copolymer were self-assembled into nanospheres. After that, core of nanospheres expanded due to the continuous flow of Grignard monomer from **2** into the core of micelles. At this stage, increasing DP of PT for *o*-Tol-P3HT-*b*-PT only caused the core expansion of micelles (Figure 3.14a). However, increasing DP of PT for P3HT-*b*-PT caused PT defect on the shell due to the triblock copolymer formation as well as core expansion (Figure 3.14b), which could allow for the formation of ill-defined 1D nanorod with occasional branching (Figure 3.13b and 3.14b). Moreover, this triblock copolymer formation reduced the DP of PT participating the core formation.

Conclusion

In situ nanoparticlization of P3HT₅₀-*b*-PT₄₀ and *o*-Tol-P3HT₅₀-*b*-PT₄₀ formed short 1D nanoparticles. NPs from *o*-Tol-P3HT₅₀-*b*-PT₄₀ were well-defined short 1D nanoparticles without branching. However, NPs from P3HT₅₀-*b*-PT₄₀ were ill-defined short 1D nanoparticles with occasional branching. The difference of the shape of NPs from *o*-Tol-P3HT₅₀-*b*-PT₄₀ and P3HT₅₀-*b*-PT₄₀ could be originated from the different initiation system, i.e. external initiation *versus* internal initiation.

References

- (1) Yoon, K.-Y.; Lee, I.-H.; Kim, K. O.; Jang, J.; Lee, E.; Choi, T.-L. *J. Am. Chem. Soc.* **2012**, *134*, 14291.
- (2) Kim, J.; Kang, E.-H.; Choi, T.-L. *ACS Macro Lett.* **2012**, *1*, 1090.
- (3) Lee, I.-H.; Amaladass, P.; Yoon, K.-Y.; Shin, S.; Kim, Y.-J.; Kim, I.; Lee, E.; Choi, T.-L. *J. Am. Chem. Soc.* **2013**, *135*, 17695.
- (4) Lee, I.-H.; Amaladass, P.; Choi, T.-L. *Chem. Commun.* **2014**, *50*, 7945.
- (5) Yoon, K.-Y.; Lee, I.-H.; Choi, T.-L. *RSC Adv.* **2014**, *4*, 49180.
- (6) Yoon, K.-Y.; Shin, S.; Kim, Y.-J.; Kim, I.; Lee, E.; Choi, T.-L. *Macromol. Rapid Commun.* **2015**, *36*, 1069.
- (7) Shin, S.; Yoon, K.-Y.; Choi, T.-L. *Macromolecules* **2015**, *48*, 1390.
- (8) The paper for in situ nanoparticlization of PPP-*b*-P3MT was recently submitted.

- (9) Loewe, R. S.; Ewbank, P. C.; Liu, J.; Zhai, L.; McCullough, R. D. *Macromolecules* **2001**, *34*, 4324.
- (10) Patra, S. K.; Ahmed, R.; Whittell, G. R.; Lunn, D. J.; Dunphy, E. L.; Winnik, M. A.; Manners, I. *J. Am. Chem. Soc.* **2011**, *133*, 8842.
- (11) Brown, P. J.; Thomas, D. S.; Köhler, A.; Wilson, J. S.; Kim, J.-S.; Ramsdale, C. M.; Siringhaus, H.; Friend, R. H. *Phys. Rev. B* **2003**, *67*, 064203.
- (12) Samitsu, S.; Shimomura, T.; Heike, S.; Hashizume, T.; Ito, K. *Macromolecules* **2008**, *41*, 8000.
- (13) Tkachov, R.; Senkovskyy, V.; Komber, H.; Sommer, J.-U.; Kiriya, A. *J. Am. Chem. Soc.* **2010**, *132*, 7803.
- (14) Verswyvel, M.; Monnaie, F.; Koeckelberghs, G. *Macromolecules* **2011**, *44*, 9489.

Chapter 4

Pd-Fe₃O₄ heterodimer nanocrystal-catalyzed Suzuki-Miyaura polycondensation

Introduction

Organometallic chemistry has been widely used for the ‘cut and sew’ of chemical bonds. Significantly, palladium (Pd) is one of the most widely used source of catalysts due to its cheap price, abundance, stability, and easy modulation of its catalyzing ability. One excellent example is Pd-catalyzed Suzuki-Miyaura C-C coupling reaction, which greatly contributed to the era of organic electronics. Particularly, Pd(0) (or Pd(II)) in combination with specific phosphine ligands became a powerful tool to pave the way for the success of Suzuki-Miyaura reaction. However, even though the homogeneous Pd-L_n (where L is ligand) catalysts have been highly being useful in C-C bond formation reaction, poor recyclability of homogeneous catalyst and use of expensive ligand systems are still challenging. To address these challenges, recyclable, ligand-free, and well-defined heterogeneous catalysts were recently being appeared in the field of C-C bond forming reactions such as Heck, Stille, and Suzuki-Miyaura reactions. However, even with the success of heterogeneous catalysis, surprisingly, these catalysts have not been applied to polymerization, especially for the synthesis of conjugated polymers, except for very recent only one example using Pd/C as catalyst.¹ Moreover, although, conjugated polymers were synthesized by Pd/C catalyst, recycling of Pd/C catalyst was totally failed.¹ Thus, to overcome the previous limitations, we envisioned that recently developed heterogeneous Pd-Fe₃O₄ catalyst with well-defined heterodimer structure would be an excellent candidate for the synthesis of conjugated polymers due to the recyclability, easy recovery, and high reactivity in small molecular Suzuki-Miyaura

reaction.²⁻⁵ In this chapter, we present Pd-Fe₃O₄ heterodimer catalyzed Suzuki-Miyaura polycondensation for the synthesis of conjugated polymers with high recyclability.

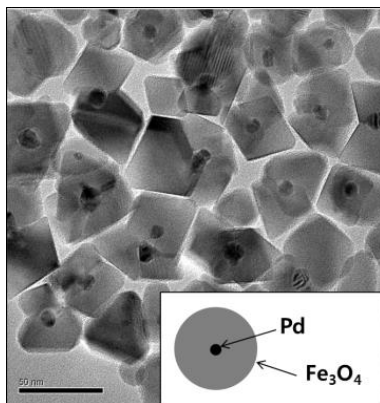
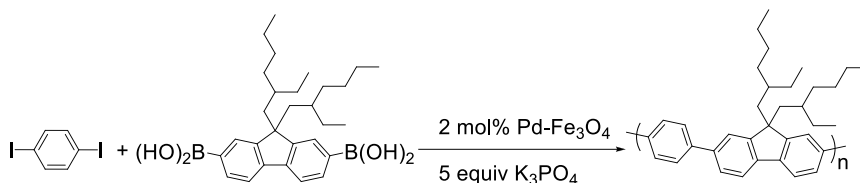


Figure 4.1. TEM images of Pd-Fe₃O₄ heterodimer nanocrystal²

Results and Discussions

Table 4.1. Optimization of Suzuki polymerization

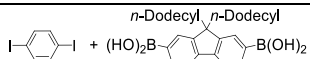
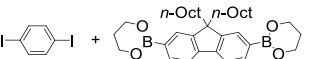
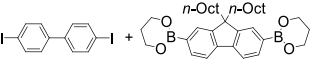
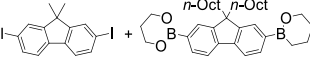
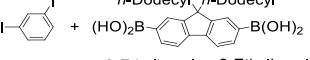
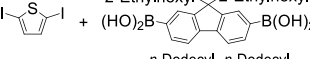
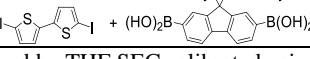


entry	Solvent	conc. (M)	temp. (°C)	M_n^a	PDI ^a	yield
1	DMF	0.10	160	4.3 k	2.07	31%
2	1,4-dioxane	0.10	105	13.0 k	2.52	84%
3	THF/H ₂ O (v/v = 3/1)	0.10	100	7.0 k	1.90	87%
4	THF	0.15	70	15.6 k	3.63	95%
5	THF	0.15	110	15.2 k	2.72	96%

^a Determined by THF SEC calibrated using polystyrene (PS) standards. M_n is given in g/mol.

Suzuki-Miyaura polymerization of *p*-diiodobenzene and 2,7-diboronic acidfluorene was performed in the presence of 2 mol% Pd-Fe₃O₄ heterodimer catalyst and 5 equiv. K₃PO₄ with various of reaction solvent and temperatures. Among the tested reaction conditions, the polymerization showed the highest number average molecular weight (M_n) with high yield when it was catalyzed in anhydrous THF at 70 °C or 110 °C (Table 4.1, entries 4 and 5). It was reported that Suzuki-Miyaura coupling reaction sometimes occurred in anhydrous condition, however, even in this case, ppm amount of water could be important for the reaction. Although small amount of water could be important for the polymerization, it is interesting that addition of extra water reduced the M_n from 15 to 7 kg/mol (Table 4.1, entry 3), because the catalyst was not dispersed in reaction medium but attached to the wall of reaction vessel.

Table 4.2. Synthesis of conjugated polymers using Pd-Fe₃O₄ catalyst at 70 °C

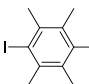
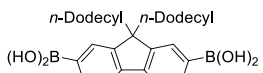
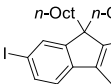
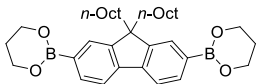
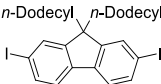
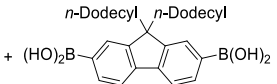
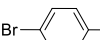
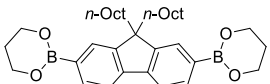
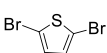
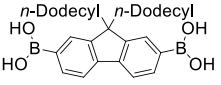
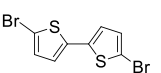
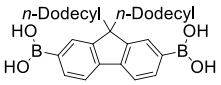
entry	monomers	M_n^a	PDI ^a	yield
1		16.2 k	2.90	>99%
2		19.5 k	3.32	78%
3		27.1 k	2.72	74%
4		10.7 k	2.21	99%
5		14.9 k	2.47	>99%
6 ^b		13.0 k	3.62	85%
7		20.2 k	3.33	95%

^a Determined by THF SEC calibrated using PS standards. M_n is given in g/mol.

^b Reaction was run at 110 °C.

With the optimization condition in hand, we started to expand the substrate scope for the polymerization. The reaction was catalyzed smoothly with boronic ester analogue as well as boronic acid fluorene (Table 4.2, entries 1 and 2). Moreover, diiodo compound of biphenyl, fluorene, thiophene, and bithiophene also underwent polymerization with M_n ranging from 10 to 27 kg/mol with moderate to high yield (Table 4.2, entries 3-7). It is noteworthy that bithiophene unit was successfully incorporated into the polymer to give F12T2, the didodecyl derivative of the well-known polymer, poly(9,9-dioctylfluorene-*alt*-bithiophene) (F8T2), for organic thin film transistor (OTFT) applications.⁶ All the polymers dissolved quite well in common organic solvents such as THF and chloroform.

Table 4.3. Polymerization trial with bromide or sterically bulky iodide compounds

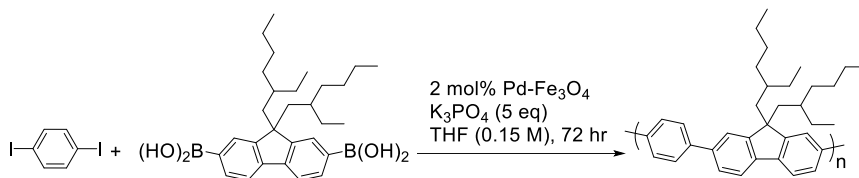
entry	monomers	M_n^a	PDI ^a	yield
1	 + 	2.5k	1.20	80%
2 ^b	 + 	4.3k	1.58	90%
3	 + 	trace amount		
4	 + 	trace amount		
5	 + 	trace amount		
6	 + 	n.d.		13%

^a Determined by THF SEC calibrated using PS standards. M_n is given in kg/mol.

^b Reaction was run at 110 °C.

Although the polymerization underwent smoothly with diiodo compounds such as *p*-diiodobenzene, the polymerization was hampered when sterically demanding diiodo compounds (Table 4.3, entries 1-3) or dibromo compounds such as *p*-dibromobenzene and 2,5-dibromothiophene were used (Table 4.3, entries 4-6). This low reactivity of dibromo compounds was also observed in small molecule Suzuki-Miyaura reaction.²

Table 4.4. Recycling of the Pd-Fe₃O₄ HNC catalyst *with* and *without* sonication process



(a) recycling at 70 °C (w/ sonication)

run	temp. (°C)	<i>M_n</i> ^a	PDI ^a	yield	ICP- MS (ppm)
1	70	17.6k	4.03	>99%	38
2	70	14.2k	3.12	95%	17
3	70	8.6k	2.34	95%	38
4	70	12.6k	4.93	77%	28
5	70	11.3k	2.42	>99%	31
6	70	6.2k	3.82	34%	n.d.
7	70	7.0k	4.53	52%	n.d.
8	70	21.5k	3.05	81%	n.d.
9	70	14.1k	3.43	65%	n.d.
10	70	21.8k	7.99	82%	n.d.
11	70	15.1k	2.14	>99%	n.d.

(b) recycling at 110 °C (w/ sonication)

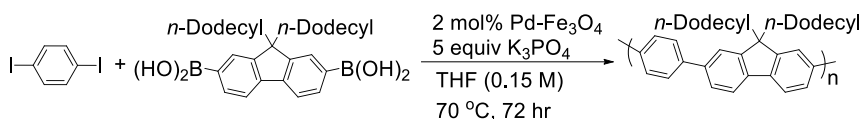
run	temp. (°C)	<i>M_n</i> ^a	PDI ^a	yield	ICP- MS (ppm)
1	110	8.2k	2.37	80%	56
2	110	15.9k	2.83	94%	3
3	110	11.9k	2.94	87%	24
4	110	8.1k	2.19	90%	4
5	110	4.3k	1.58	47%	n.d.
6	110	13.0k	3.12	86%	21
7	110	9.2k	2.78	80%	n.d.
8	110	5.8k	2.00	56%	n.d.
9	110	9.1k	2.24	68%	n.d.
10	110	14.6k	3.14	85%	n.d.

(c) recycling at 70 °C (w/o sonication)

run	temp. (°C)	<i>M_n</i> ^a	PDI ^a	yield	ICP- MS (ppm)
1	70	15.6k (22.6k) ^b	3.63 (2.44) ^b	95% (84%) ^b	53 (32) ^b
2	70		n.d.	26%	n.d.
3	70		n.d.	17%	n.d.

^a Determined by THF SEC calibrated using PS standards. *M_n* is given in g/mol.

^b Determined after Soxhlet extraction with methanol and acetone.

Table 4.5. Recycling of Pd-Fe₃O₄ HNC catalyst for Suzuki polymerization

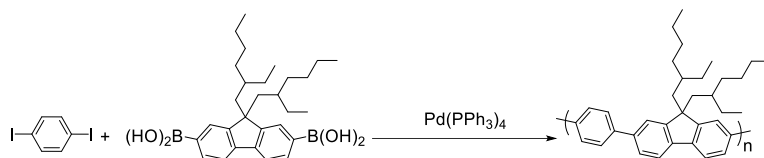
Run	M_n^a	PDI ^a	yield	Pd _{re} ^b
1	16.2 k	2.90	>99%	52 ppm
2	19.9 k	2.49	>99%	28 ppm
3	17.5 k	2.82	98%	21 ppm
4	15.3 k	2.41	>99%	5 ppm
5	18.9 k	2.49	94%	34 ppm
6	11.3 k	2.35	>99%	17 ppm
Average	16.5 k	-	>98%	26 ppm

^a Determined by THF SEC calibrated using PS standards. M_n is given in g/mol.

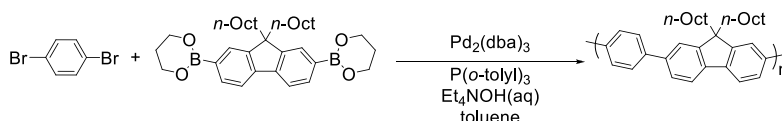
^b Concentration of residual Pd in polymers detected by inductively coupled plasma-mass spectrometry (ICP-MS)

To examine the recycle ability of Pd-Fe₃O₄ heterodimer catalyst under optimized condition, the polymerization underwent both of temperatures at 70 °C and 110 °C (Table 4.4 and Table 4.5). It is noteworthy that sonication prior to the polymerization was critical to succeed the polymerization with recycled catalyst (Table 4.4a and c). Overall, the polymerization underwent at least 6 times without losing its activity at both temperatures (Table 4.4a and b and Table 4.5). Moreover, ICP-MS indicated that residual Pd level after the polymerization was quite low (4-56 ppm) (Table 4.4 and Table 4.5), suggesting relatively clean catalysis in comparison with homogeneous Pd catalyst system (Table 4.6).

Table 4.6. Homogeneous Pd(PPh₃)₄ and Pd₂(dba)₃-catalyzed Suzuki polymerization



entry	solvent	Pd(PPh ₃) ₄ loading	Base	time (hr)	temp (°C)	<i>M_n</i> ^a	PDI ^a	yield	ICP-MS (ppm)
1	THF (0.15 M)	2 mol%	K ₃ PO ₄ (5 eq)	72	70	4.3k	1.88	73%	1996



entry	solvent	Pd ₂ (dba) ₃ loading	Base	time (hr)	temp (°C)	<i>M_n</i> ^a	PDI ^a	yield	ICP-MS (ppm)
2	toluene (0.15 M)	2 mol%	Et ₄ NOH (7 eq)	87	110	8.5k (9.9k) ^b	2.76 (2.66) ^b	69% (62%) ^b	151 (101) ^b

^a Determined by THF SEC calibrated using PS standards. *M_n* is given in g/mol

^b Determined after Soxhlet extraction with methanol and acetone.

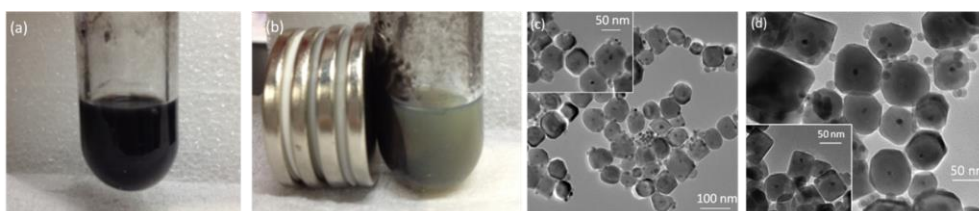


Figure 4.2. Recovery of Pd-Fe₃O₄ HNC using external magnet after polymerization

(a) without magnet (b) with magnet. TEM images of Pd-Fe₃O₄ HNC after recycling reactions in Table 4.4 (a). (c) before reaction (d) after 5 runs of recycling reactions (inset : after 11 runs of recycling reactions). Smaller and darker particle is Pd and larger and lighter particle is Fe₃O₄.

Ferrimagnetic property of Pd-Fe₃O₄ heterodimer made recycling of catalyst easy by using external magnet (Figure 4.2a and b). Moreover, after the 11 times of recycling polymerization, the heterodimer structure of Pd-Fe₃O₄ was maintained as confirmed by TEM imaging, indicating robustness of Pd-Fe₃O₄ (Figure 4.2c and d).

Conclusion

In summary, we demonstrated successful Suzuki-Miyaura polymerization using Pd-Fe₃O₄ heterodimer catalyst. The polymerization condition was optimized with the choice of solvent, base, and temperatures. In particular, the polymerization underwent quite well with moderate to high molecular weight and high yield under anhydrous condition. The recycling of catalyst was successfully done 11 times, and dispersion of Pd-Fe₃O₄ catalyst by sonication was important to succeed the recycling process. Residual Pd level in conjugated polymers was relatively 100 times lower than its homogeneous analogue system. We believe that this new heterogeneous catalyst will open a new way to form conjugated polymers with high purity and high economy.

References

- (1) Liu, S.-Y.; Li, H.-Y.; Shi, M.-M.; Jiang, H.; Hu, X.-L.; Li, W.-Q.; Fu, L.; Chen, H.-Z. *Macromolecules* **2012**, *45*, 9004.
- (2) Jang, Y.; Chung, J.; Kim, S.; Jun, S. W.; Kim, B. H.; Lee, D. W.; Kim, B. M.; Hyeon, T. *Phys. Chem. Chem. Phys.* **2011**, *13*, 2512.

- (3) Chung, J.; Kim, J.; Jang, Y.; Byun, S.; Hyeon, T.; Kim, B. M. *Tetrahedron Lett.* **2013**, *54*, 5192.
- (4) Lee, J.; Chung, J.; Byun, S. M.; Kim, B. M.; Lee, C. *Tetrahedron* **2013**, *69*, 5660.
- (5) Byun, S.; Chung, J.; Jang, Y.; Kwon, J.; Hyeon, T.; Kim, B. M. *RSC Adv.* **2013**, *3*, 16296.
- (6) Sirringhaus, H.; Kawase, T.; Friend, R. H.; Shimoda, T.; Inbasekaran, M.; Wu, W.; Woo, E. P. *Science* **2000**, *290*, 2123.

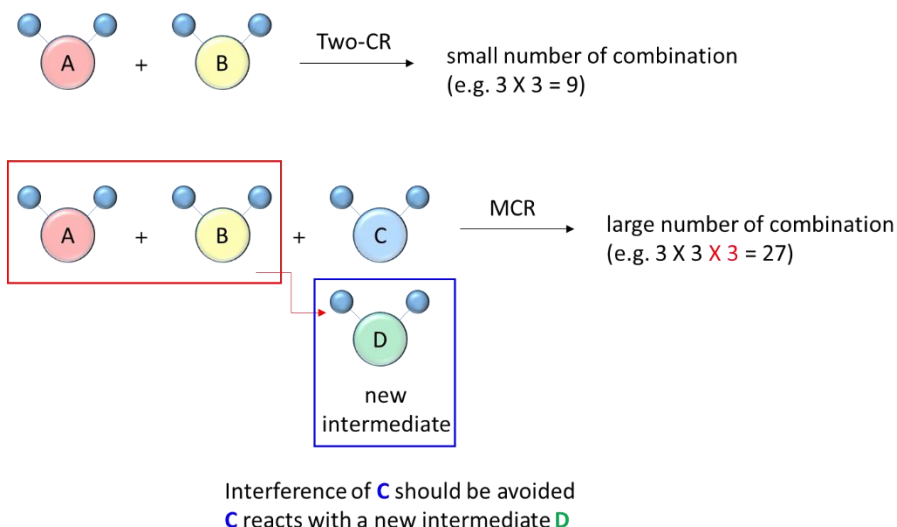
Chapter 5

Cu-catalyzed multicomponent polymerization: Synthesis of poly(*N*-sulfonylamidine)

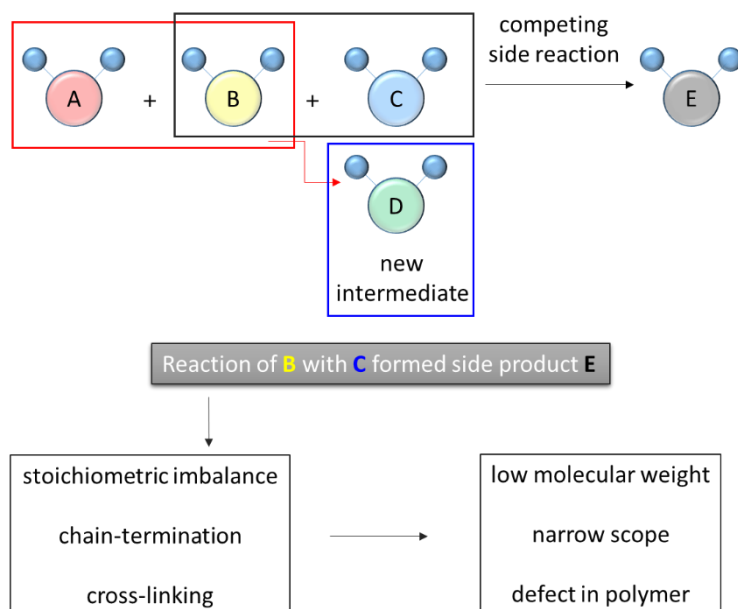
Introduction

Multi-component reaction is an approach to construct complex molecular structures from three or even larger number of molecules in one-pot. For example, Cu-catalyzed three-component reaction (3CR),¹ the Mannich reaction,² the Passerini reaction,³ and A³-coupling,⁴ have been reported enabling fast, step-economic, and efficient formation of complex small molecules. Moreover, it is noteworthy to make it a point that the combinatorial approach of all monomers being able to build a library of complex small molecules in efficient way (Scheme 5.1.), which might be important for screening system in chemical biology and so on. At this moment, we turned our attention into the multi-component polymerization (MCP), which has not been much studied compared to multi-component reactions. The reason why it has not been studied much was basically saying that it needs highly efficient (>95% conversion) and selective reactions to synthesize polymers. Even small extent of side reactions could interfere whole multi-component polymerization process (Scheme 5.2.). For example, stoichiometric imbalance, chain-termination, and cross-linking from side reactions would result in low molecular weight, narrow substrate scope, and defects in polymer structures (Scheme 5.2.). Herein, we reported a new multi-component polymerization overcoming these challenges observed in previous reports.⁵⁻¹¹ With careful optimization, we successfully synthesized poly(*N*-sulfonylamidine)s with defect-free, high molecular weight, large substrate scope, and via Cu-catalyzed multi-component polymerization.

Scheme 5.1. Comparison between two and multi-component reactions (MCR)

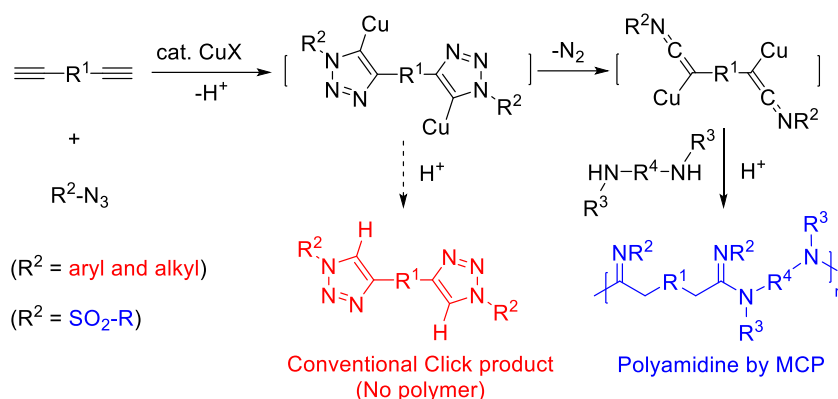


Scheme 5.2. Impact of side reactions on multi-component polymerization (MCP)



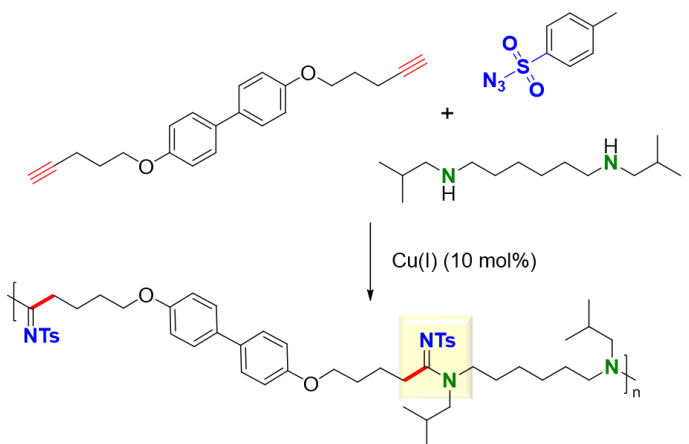
Results and Discussions

Scheme 5.3. Polymerization Scheme for Poly(*N*-sulfonylamidine) Synthesis



As an exemplary system for multi-component polymerization overcoming previous limitations, we choose Cu-catalyzed multi-component reaction for the synthesis of poly(*N*-sulfonylamidine)s.^{1a} This reaction was quite unique Click reaction in that Cu-bound triazole ring intermediates open to generate ketenimine species which were highly reactive with amine nucleophiles (Scheme 5.3). Whereas, conventional Click reaction only formed triazole ring that was obtained by proton quenching of Cu-bound triazole ring species (Scheme 5.3). To drive the polymerization efficiently, Cu-bound triazole ring should be opened quantitatively to form ketenimine species, and that was achievable by using electron-deficient sulfonyl azides (Scheme 5.3).¹

Table 5.1. MCP Optimization for a Model Polymer



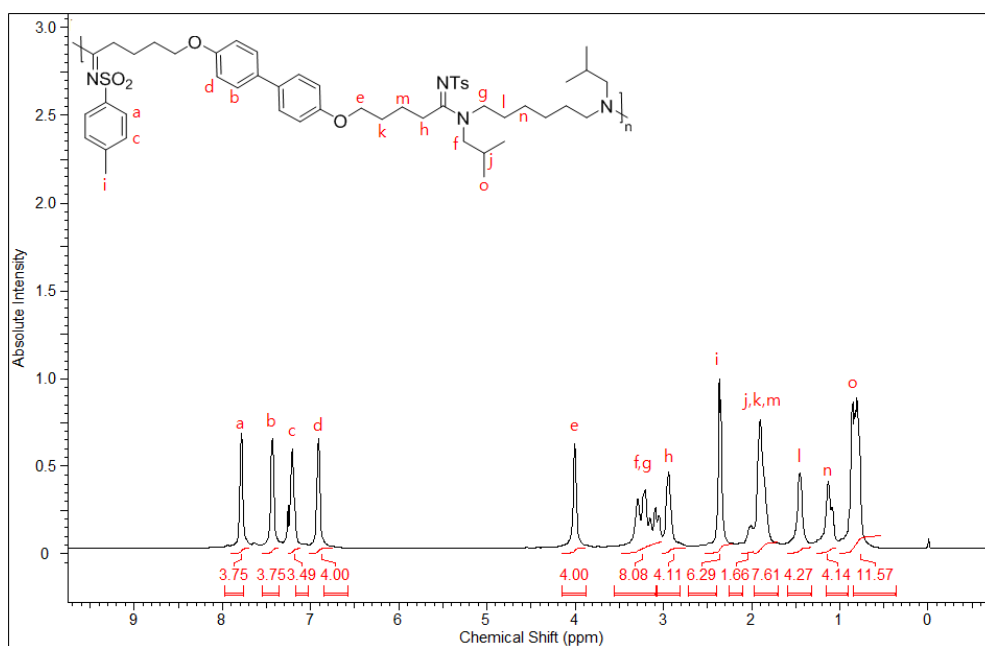
entry	catalyst	solvent	conc. (M)	temp. (°C)	additive (equiv.)	M_n (PDI) ^a
1	CuI	THF	0.5	50	None	2.7k (1.22)
2	CuI	DMF	0.5	70	None	6.2k (1.71)
3	CuCl	DMF	0.5	70	None	7.5k (1.92)
4	CuCl	DMF	1.0	70	TBTA (0.1)	7.3k (1.73)
5	CuCl	DMF	1.0	70	TEA (5)	10.8k (2.81)

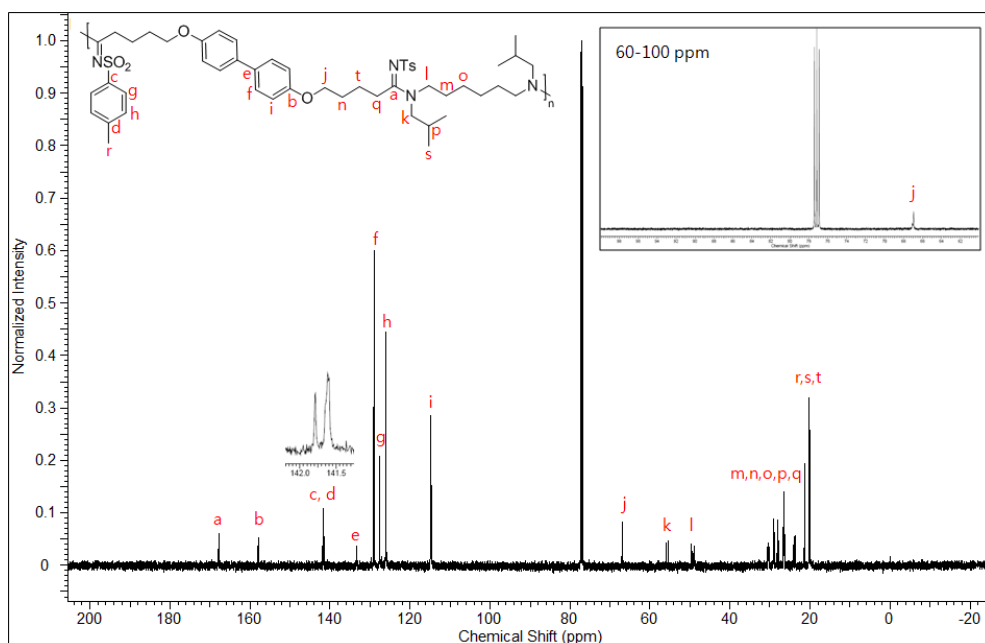
^a Determined by THF SEC calibrated by polystyrene standards.

We decided a monomer set for model polymerization, e.g. diyne shown in Table 5.1, *p*-toluenesulfonyl azide, and *N,N'*-diisobutyl-1,6-hexanediamine. First attempt for the polymerization of a model polymer was performed in optimized condition for small molecules reported by Chang's group.^{1a} However, polymerization was sluggish probably due to the solubility limit from highly polar (*N*-sulfonylamidine) functionalities inside the polymer chains (Table 5.1, entry 1). The

solubility issue was easily overcome by using polar DMF as reaction solvent. Actually, DMF was not a good solvent for small molecule multi-component reaction,^{1d} however, all of sudden, it showed better performance in that molecular weight and yield of polymers (Table 5.1, entry 2). With careful optimization of catalyst, concentration, temperature, and additive base, we decided optimal condition for the Cu-catalyzed multi-component polymerization (Table 5.1, entry 5).

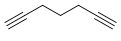
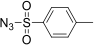
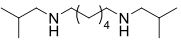
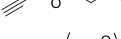
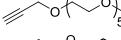
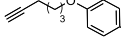
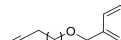
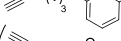
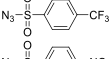
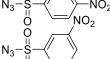
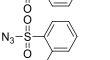
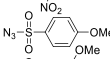
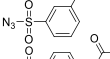
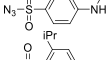
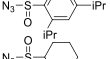
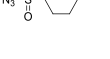

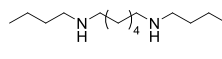
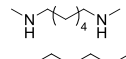
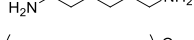
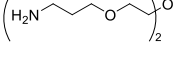
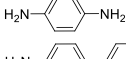
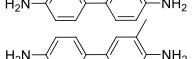
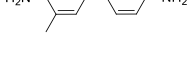
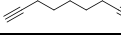
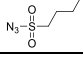
Figure 5.1. ¹H NMR and ¹³C NMR spectra of the model polymer





The resulting model poly(*N*-sulfonylamindines) was analyzed by ^1H and ^{13}C NMR spectroscopy. The sharp peaks shown in ^1H NMR spectrum is an indicative of highly regular polymer structures (Figure 5.1). Moreover, assignment of NMR spectroscopy data for model poly(*N*-sulfonylamindines) suggested that polymers have well-defined structures without any defect (Figure 5.1). This is also indicating that very highly selective multi-component polymerization occurred without conventional Click reaction (Scheme 5.3 and Figure 5.1).

Table 5.2. Synthesis of Various Poly(*N*-sulfonylamidines)

entry	diyne	sulfonyl azide	diamine	M_n^a (MALLS) ^b	PDI ^a	yield ^c
1	1a 	2a 	3a 	4.7k (22.4k)	1.52	72%
2	1b 	2a	3a	4.8k (23.4k)	1.54	98%
3	1c 	2a	3a	6.2k (22.8k)	1.50	79%
4	1d 	2a	3a	16.7k (56.1k)	2.99	84%
5	1e 	2a	3a	18.2k (63.9k)	2.53	78%
6	1f 	2a	3a	10.8k (30.8k)	2.81	76%
7	1f	2b 	3a	11.1k (21.5k)	2.16	74%
8	1f	2c 	3a	14.6k (-) ^d	3.51	90%
9	1f	2d 	3a	16.8k (-) ^d	5.07	85%
10	1f	2e 	3a	15.3k (-) ^d	5.92	90%
11	1f	2f 	3a	12.2k (20.1k)	1.85	87%
12	1f	2g 	3a	10.7k (25.7k)	1.51	93%
13	1f	2h 	3a	23.5k (-) ^d	1.77	91%
14	1f	2i 	3a	13.2k (44.7k)	1.69	78%
15	1f	2j 	3a	7.4k (34.6k)	2.77	66%
16	1f	2a	3b 	13.3k (19.9k)	2.97	74%
17	1f	2i	3b	9.7k (43.6k)	1.93	72%
18	1f	2i	3c 	8.9k (67.2k)	2.03	79%
19	1f	2i	3d 	19.2k (-) ^d	1.97	93%
20	1c	2i	3e 	14.5k (31.7k)	1.75	79%
21	1f	2i	3e	12.7k (44.0k)	2.10	77%
22	1f	2i	3f 	18.6k (75.1k)	1.91	72%
23	1f	2i	3g 	15.7k (-) ^d	2.37	76%
24	1c	2i	3h 	8.3k (50.9k)	1.73	71%
25	1f	2i	3h	15.7k (74.9k)	1.53	72%
26	1g 	2k 	3h	15.0k (-) ^d	1.99	86%

^a Determined by DMF SEC calibrated by poly(methyl methacrylate) standards (entries 5, 7–14, 16–19, 21–23, 25–26). Determined by THF SEC calibrated by polystyrene standards (entries 1–4, 6, 15, 20, 24).

^b Absolute molecular weight was determined by THF SEC (CHCl₃ SEC for entries 11 and 12) using an MALLS detector.

^c Isolated yield after precipitation from selected solvents.

^d Absolute molecular weight could not be obtained because polymers were not soluble in THF and CHCl₃.

With optimized condition in hand, we broaden substrate scope by changing each monomer structures (Table 5.2). We choose sorts of monomers as shown in Table 5.2, e.g. seven diynes, eleven sulfonyl azides, eight diamines. Theoretically, it could be possible to generate 616 ($7 \times 11 \times 8 = 616$) different polymers. However, to show its robustness, it is enough to demonstrate some of examples. To describe the power for the construction of poly(*N*-sulfonylamidine) using Cu-MCP, 26 examples (quite large entries among papers published in polymer community) were successfully demonstrated (Table 5.2). Basically saying that, the polymerization occurred very smoothly with high molecular weight (up to 75 kg/mol) regardless of the steric and electronic factors of monomers (Table 5.2).

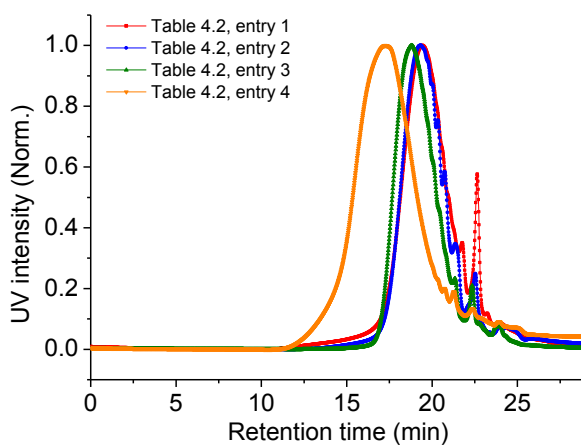


Figure 5.2 THF SEC trace monitored by UV Detector (254 nm)

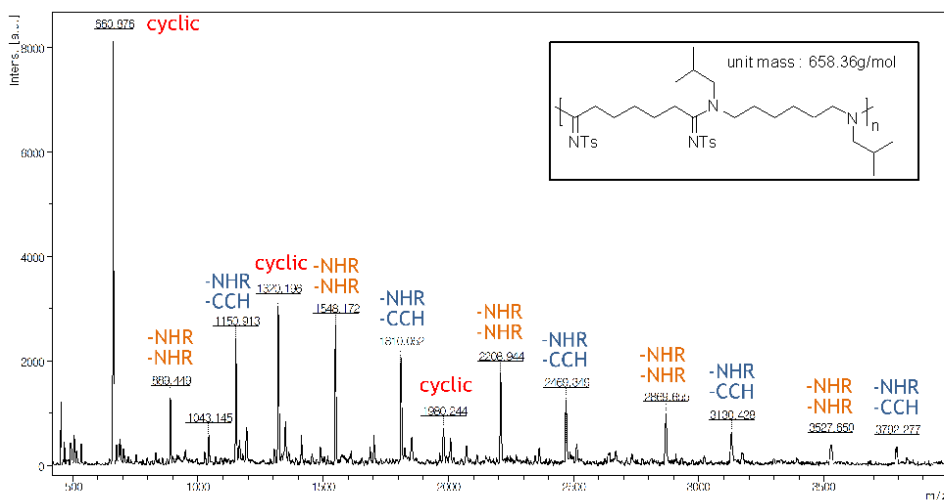


Figure 5.3. MALDI-TOF analysis of the model polymer

Detail analyses of resulting polymers using MALDI-TOF and SEC showed that cyclization during step-growth polymerization inevitably occurred, which reduced molecular weight of polymers (Figure 5.2 and Figure 5.3). To reduce cyclization of polymers, not only the concentration for polymerization increased (Table 5.1), but also monomer structures were engineered (Table 5.2). Specifically, long and rigid diyne and diamine structures afforded polymers with minimal amount of cyclic product (Figure 5.2).

Conclusion

In conclusion, we have been demonstrated highly robust and efficient Cu-catalyzed multicomponent polymerization for the synthesis of poly(*N*-sulfonylamidines). The polymerization condition was optimized with careful choice of solvent, catalyst, and additives. Among those factors, DMF as solvent and excess amount of TEA as base were critical to improve the polymerization. Moreover, using optimal condition, we constructed 26 well-defined polymers with high molecular weight and moderate to high yield. This Cu-catalyzed multi-component polymerization overcome previous limitations such as low molecular weight, narrow substrate scope, and defect in polymer chains.

References

- (1) (a) Bae, I.; Han, H.; Chang, S. *J. Am. Chem. Soc.* **2005**, *127*, 2038. (b) Yoo, E. J.; Bae, I.; Cho, S. H.; Han, H.; Chang, S. *Org. Lett.* **2006**, *8*, 1347. (c) Yoo, E. J.; Ahlquist, M.; Bae, I.; Fokin, V. V.; Sharpless, K. B.; Chang, S. *J. Org. Chem.* **2008**, *73*, 5520. (d) Kim, J. Y.; Kim, S. H.; Chang, S. *Tetrahedron Lett.* **2008**, *49*, 1745. (e) Hwang, S. J.; Cho, S. H.; Chang, S. *Pure Appl. Chem.*, **2008**, *80*, 873. (f) Kim, S. H.; Park, S. H.; Choi, J. H.; Chang, S. *Chem. Asian J.* **2011**, *6*, 2618.
- (2) (a) Mannich, C.; Krosche, W. *Arch. Pharm* **1912**, *250*, 647. (b) Arend, M.; Westermann, B.; Risch, N. *Angew. Chem., Int. Ed.* **1998**, *37*, 1044.
- (3) (a) Passerini, M. *Gazz. Chem. Ital.* **1921**, *51*, 126. (b) Andreana, P. R.; Liu, C. C.;

Schreiber, S. L. *Org. Lett.* **2004**, *6*, 4231.

(4) Peshkov, V. A.; Pereshivko, O. P.; Van der Eycken, E. V. *Chem. Soc. Rev.* **2012**, *41*, 3790.

(5) Kreye, O.; Tóth, T.; Meier, M. A. R. *J. Am. Chem. Soc.* **2011**, *133*, 1790.

(6) Deng, X. X.; Li, L.; Li, Z. L.; Lv, A.; Du, F. S.; Li, Z. C. *ACS Macro Lett.* **2012**, *1*, 1300.

(7) (a) Takenoya, K.; Yokozawa, T. *Macromolecules* **1998**, *31*, 2906. (b) Niimi, L.; Shiino, K.; Hiraoka, S.; Yokozawa, T. *Macromolecules* **2002**, *35*, 3490.

(8) Ihara, E.; Hara, Y.; Itoh, T.; Inoue, K. *Macromolecules* **2011**, *44*, 5955.

(9) Niimi, L.; Serita, K.; Hiraoka, S.; Yokozawa, T. *J. Polym. Sci., Part A: Polym. Chem.* **2002**, *40*, 1236.

(10) Ochiai, B; Ogihara, T; Mashiko, M; Endo, T. *J. Am. Chem. Soc.* **2009**, *131*, 1636.

(11) (a) Miyaki, N.; Tomita, I.; Endo, T. *Macromolecules* **1997**, *30*, 4504. (b) Choi, C. K.; Tomita, I.; Endo, T. *Macromolecules* **2000**, *33*, 1487. (c) Ishibe, S.; Tomita, I. *J. Polym. Sci., Part A: Polym. Chem.* **2005**, *43*, 3403. (d) Nakagawa, K.; Tomita, I. *Chem. Lett.* **2007**, *36*, 638. (e) Siamaki, A. R.; Sakalauskas, M.; Arndtsen, B. A. *Angew. Chem., Int. Ed.* **2011**, *50*, 6552.

(12) (a) Nastruzzi, C.; Gambari, R.; Menegatti, E.; Walde P.; Luisi, P. L. *J. Pharm. Sci.* **1990**, *79*, 672. (b) Sharavanan, K.; Komber, H.; Fischer, D.; Böhme, F. *Polymer*, **2004**, *45*, 2127.

국문 초록

고분자의 합성과 자기 조립 현상을 효율적으로 조절하여 원하는 구조를 만들어내는 것은 기능성 나노 물질 개발에 있어 핵심적 기초를 담당한다. 이 논문의 다음 네 개의 단원에서, 고분자 합성과 자기 조립 현상을 손쉽게 효율적으로 조절할 수 있는 방법론에 대해 소개하고자 한다.

단원 2에서, 전도성 고분자의 직접적 자기조립 현상에 대해 보고한다. 이 단원에서는 나노 구조의 핵 부분 (core)을 형성하는 고분자의 구조가 나노 구조를 어떻게 조절 할 수 있는지에 대해 논의 한다. 하나의 모델 시스템으로서, poly(*para*-phenylene) 과 polythiophene 의 블록 공중합체에 대한 연구를 바탕으로 하였다.

단원 3에서, 전도성 고분자의 직접적 자기조립 현상에 영향을 미치는 요인으로서, 블록 공중합체의 첫 번째 블록의 영향을 알아본다. 단원 2와 연결 지어, poly(*para*-phenylene)을 poly(3-alkylthiophene)으로 바꾸었을 때, 나노 구조에 어떤 변화가 있는지를 확인하였다.

단원 4에서, Pd-Fe₃O₄ 나노 결정체를 이용하여, Suzuki-Miyaura 고분자 합성법을 시도한 연구를 기술하였다. 나노 결정체로 전도성 고분자를 합성 할 수 있었으며, 나노 결정체는 재사용이 가능한 것을 보였다.

단원 5 에서, 구리 촉매를 이용한 다분자 반응을 이용해 고분자를 합성한 예를 보고한다. 다양한 고분자를 짧은 시간에 다량으로 합성할 수 있는 방법을 제시하고, 실제 성공 사례를 기술하였다.

요약하면, 이 논문에서는 고분자의 합성과 자기 조립 현상을 효율적이고 경제적으로 할 수 있는 방법들에 대해 기술하였다. 그러한 예로서, 전도성 고분자의 직접적 자기 조립 현상, 재사용이 가능한 heterogeneous 촉매를 이용한 고분자 합성, 다분자 반응을 이용한 고분자 합성에 대해 기술하였다. 여기에 소개된 전략들이 더 발전되어, 새로운 유용한 나노 구조체 형성에 도움이 되기를 바란다.

주요어 : 전도성 고분자의 직접적 자기 조립 현상, 재사용이 가능한 heterogeneous 촉매를 이용한 고분자 합성, 다분자 반응을 이용한 고분자 합성

학 번 : 2010-20288